Micromagnetic study of Brownian motion in chiral magnetic structures

Fei Ye

MSc by Research

University of York

Electronics Engineering

November 2021

Abstract

A magnetic skyrmion is a type of vortex magnetic structure that is stabilized by its topological structure. An example of this type of spin structure can be found in thin magnetic films with perpendicular magnetic anisotropy and Dzyaloshinski-Moriya interactions. It has a size range between nanometers and microns, and a variety of excitation mechanisms can be used to modulate its dynamics, including electric current and electric fields. Novel spintronic storage devices can be constructed with magnetic skyrmions as a form of information carrier. Hence, magnetic bimerions can be seen as the in-plane topological counterpart of magnetic skyrmions. Despite this, there are few studies that have been able to use systematic research into spin topological features to explain their random thermal motions. In this project, a micro-magnetic method based on the Landau-Lifshitz-Gilbert equation has been used to study the dynamics of bimeron in magnetic nanodots under the influence of thermal effects. An investigation was conducted to determine the impact of anisotropy, DMI, damping, and geometric size on the Brownian motion of bimerons. According to our results, the thermal Brownian motion of the magnetic bimeron under thermal effects is different from the thermal Brownian motion of the magnetic skyrmion with symmetry protected topological states (SPT). The thermal stability of bimeron is lower than that of magnetic skyrmion as a result of its lack of topology protection and rotational symmetry. This study contributes to the understanding of the dynamics of topological magnetic structures and provides some recommendations for the development and application of spintronic devices in the future.

Contents:

List of Figures:

Declaration of Authorship:

I declare that this thesis titled, “Micromagnetic study of Brownian motion in chiral magnetic structures”, and the work presented in it are my own.

This work has not previously been presented for an award at this, or any other, University. All sources are acknowledged as References.

Introduction

Spintronics aims to develop next generation electronic devices that rely on the intrinsic properties of electrons rather than the properties of their charges. The subject of this study is an important one in condensed matter physics, including electron transport. Electrons have two spin components of half their size in either direction. In the conductor, electron spin is random, and there is no macroscopically apparent state of spin. In macroscopic terms, ferromagnetic materials appear magnetic due to the Heisenberg exchange interaction, which aligns the spins of unpaired electrons in the same direction. Due to the discovery of the giant magneto resistance effect in multilayer magnetic thin films[1], it is now possible to influence the electron spin transport in magnetic materials by applying an external magnetic field, therefore affecting the charge transport. By applying the giant magneto resistor effect to the read-write magnetic head of the hard disk in the 1990s, IBM greatly improved the sensitivity of its magnetic probes. After the discovery of the tunneling magnetoresistance effect, the magneto resistance value increased even further. Additionally, the discovery of the spin moment effect and the spin-orbit moment effect confirmed the interaction between the electron spin and the local magnetization intensity. Thus, the electron spin can affect the magnetic state of magnetic materials. Currently, the field of electronic spin-based devices is becoming more diversified, such as magnetic random access memory[2], race-track memory[3], spin nano oscillator[4], spin microwave detector[5], electronic spin-based logic gate devices[6], etc. According to current spintronics research, a new generation of electronic spin-based devices will be developed through the study of the control and transport of electronic spins.

In 1962, Tony Skyrme[7] described some qualitative aspects of the interactions between particles when he introduced the concept of the skyrmion. Skyrme predicted the existence of particle-like stable field structures with topological shields[7]. In 1975, Belavin and Polyakov described a particle-like metastable state in two-dimensional ferromagnets, known as the magnetic skyrmion [8]. Due to its topological discontinuity in energy, this is a chiral spin structure with a vortex configuration that is non-trivial topologically[9]. Comparatively to a trivial magnetic structure, skyrmion exhibits higher stability. Additionally, theoretical physicists predicted the existence of skyrmions in the quantum hall state of a two-dimensional electron gas in the 1990s. In contrast, it was not until 2006 that Rößler et al.[10] established for the first time that stable skyrmion states exist widely in magnetic films or bulk materials. Among them, bulk materials include magnets with B20 lattice structures such as FeGe, MnSi, etc.

In 2009, magnetic skyrmion was first observed experimentally in a magnetic material system, namely in MnSi chiral materials[1]. Subsequently, the Heinze group[1] observed two skyrmion arrays in Fe/Ir magnetic thin films in 2011[11]. A magnetic skyrmion is nanoscale, robust and relatively stable, protected by chiral spin textures, and having two types of topological spin structures: the Néel-type and the Bloch-type. As they move from the core towards the periphery, Néel skyrmion spins rotate in parallel to radial directions, whereas in a bloch skyrmion spins rotate in radial directions starting from the core. Fert et al., winner of the Nobel Prize in Physics, used skyrmion as a storage medium in 2013. By recording their existence, it can be possible to capture the "1" and "0" of binary information, which can be read or written non-contact. Research reports have recently shown that, by using piezoelectric microscopy (PFM)[12], researchers discovered a variety of topological structures in perovskite ferroelectric thin films. It has been demonstrated that topological states with electric field control have unique electrical conduction properties, and these properties can be utilized for non-destructive writing and reading[13]. The development of scanning transmission electron microscopy (STEM) has led to the identification of nanoscale topological domains in perovskite ferroelectric thin films. The polarization topology can be stable at room temperature, without external force, with a similar magnetic spin behavior of a topological structure, is relatively straightforward to achieve behavior research and regulation[14].

As an in-plane counterpart of a magnetic skyrmion, is known in topology as the magnetic bimeron. Meron was originally proposed by De Alfaro et al. [15] as a classical solution of the Yang-Mills equation. The particle physicist meron describes a phenomenon known as quark confinement, wherein a quark can exist only in paired form and not in an independent form, such as bimeron. Phatak et al. [16] observed the meron pair in magnetic nanocrystals of the Permalloy alloy /Cr/ Permalloy. Wintz et al. [17] have also observed meron states in Co/Rh/NiFe nanocrystals. As a magnetic vortex, the meron is another topologically protected state, topologically equivalent to one-half of a skyrmion. As with vortices, meron also has a core whose core spins up or down (with respect to a given crystallographic). On the other hand, the spin is distributed along the radial direction (outwards or inwards) far from the core in the XY plane. Towards the end of the intermediate transition zone, the spin gradually shifts from the Z-direction into the plane. The topological number of magnetic bimerons is similar to skyrmions, which are topological spin textures with topological number $N = \frac{1}{4\pi}\int \boldsymbol{n} \cdot \left(\frac{\partial \boldsymbol{n}}{\partial x} \times \frac{\partial \boldsymbol{n}}{\partial y}\right) \mathrm{d}x\mathrm{d}y$ (where $\boldsymbol{n} = \frac{\boldsymbol{M}}{|\boldsymbol{M}|}$ and $\boldsymbol{M}$ is the magnetic moment). The topological number of Meron is $N = \pm 1/2$, which is related to the polarity of the nucleus. Meron's topological density distribution is also located near the center of its radius. One of the key differences between bimerons and skyrmions is the peripheral spin texture of the former. The spin textures on the bimerons are aligned in the inplane, whereas those on the skyrmions are pointing out of the plane. The meron possesses two topological charges, one of which is $N = +1/2$ and the other is $N = -1/2$, as a result of which these spin textures can interact strongly together.

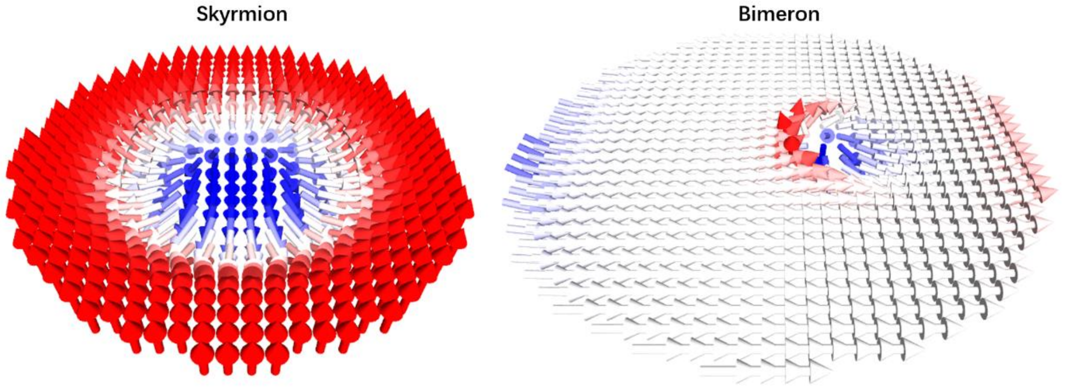

Figure 1.1 The differences in structure between skyrmion and bimeron.

According to recent research, skyrmion may serve as an ideal carrier of information in the future for spintronic devices. This structure has unique topological properties, is small, easy to drive, and is stable. A 2009 experiment led to the discovery of the properties and applications of skyrmion. Since then, research into its properties and applications has become a major focus. However, there are still a number of scientific and technical challenges to overcome before its practical application can be made. A bimeron is a spin structure with an integer topological charge, which is analogous to the skyrmion in an easy-plane magnet. On the other hand, a $N = +1$ skyrmion, compared with a meron and a bimeron, will induce a Magnus force and then are subject to the Hall effect. For example, different particles moving along an isotropic ferromagnetic track will exhibit different behaviors due to their rigidity, structural differences, and small changes in mass[18]. It is crucial for practical applications that a bimeron can be controlled to create and operate according to a topological spin structure.

So far, the writing, operating, and reading functions required by the skyrmion as an information carrier have been independently verified in experiments. Nevertheless, some of these experiments must be carried out at low temperatures. To illustrate, the Wiescountry team[19] used STM to observe and read the skyrmion or used the skyrmion array[14]. In recent years, skyrmion has been found in various materials structures at room temperature[20, 21]. For nucleation and detection, it still relies on

LTEM, MFM, and other external experimental equipment. As mentioned previously, one of the challenges will be to integrate the generation, transport, and detection of a single skyrmion into a single micro-nano electronic device at room temperature.

Thus, the generation, transport, and detection of a single skyrmion using electrical methods at room temperature and integrated into a single micro-nano electronic device is a major challenge. Yan Zhou (2019) studied the Brownian motion of skyrmion at room temperature using a polar-magneto-optical effect (MoKE) microscope with time and space resolution[22].

As discussed above, the Brownian motion of bimeron in a high-temperature environment is not clear yet. So the high-temperature Brownian motion of bimeron is the research direction of this paper. To show the difference between bimeron and skyrmions, this paper will compare them under the same conditions.

The purpose of this work is to give a stability and brownian motion comparsion between skyrmion and bimeron, under the same conditions, such as DMI, anisotropic strength and temperature. Despite the topological equivalence between the skyrmion and the bimeron soliton, their magnetic static and dynamical properties are distinct. In chapter 3, we investigate the influence of thermal effects on solitons and bi-solitons by using finite difference methods and lattice based methods. By comparing the two methods, we first determine which method is most appropriate for calculating the topological number (Q) of particles, and after that we determine the stability of particles through the calculated topological number. Using these differences, we can explain the different thermal stability of particles resulting from different topological structures. In Chapter 4, we compare the stability and thermal performance of skyrmion and bimeron microprocessors. During multiple sets of DMI and anisotropy, the position and velocity of skyrmion and bimeron are recorded, along with their instantaneous displacements and velocities. Due to the fact that the bimeron is composed of two merons, we will calculate the values for each separately. As a conclusion, we discuss the structural and topological properties of skyrmion and bimeron. By the end of this section, we discuss and compare the thermal stability and Brownian motion of skyrmion and bimeron using the topological number and mean square displacement (MSD).

Chapter.1 Fundamentals

The research involves simulation of Dzyaloshinskii-Moriya Interactions (DMI) of the type skyrmion and bimeron. In this study, the main software used is the micromagnetic simulation software MUMAX3[23], which is based on the finite-difference discretization method.

1. 1 Static micromagnetics

Maxwell's equations describe the macroscopic magnetic properties of a materials' magnetic permeability and susceptibility. The quantum mechanics describes an atomic level microscopic mechanisms and the particle theory describes magnetic properties of particles. The magnetization precession and hysteresis loop of magnetic order cannot be described by either of these two theories on a mesoscopic scale. Thus, a new theory for linking the macroscopic Maxwell's electromagnetic theory with the microscopic quantum mechanics theory becomes more necessary. This is especially true after the confirmation of the Barkhausen jump and the motion of the domain wall. Landau and Lifshitz[24] derived the domain wall structure in reverse magnetic domains in 1935. Followed by similar work published by Brown in 1940~1941[25]. In 1958, he made a report titled "Micromagnetics: Follower to Domain Theory" in an academic conference, in which the concept of micro-magnetism was first proposed[26]. Brown's equation solves the equivalent field calculation, and LL equation describes the dynamics of atomic spin moment. They make the dynamics of magnetism solvable.

According to the theory of micromagnetism, the magnetization field can be replaced by a continuous magnetization vector field $M(r)$, where $\boldsymbol{r}$ is the position vector. Thus, the vector expression of magnetization intensity in different Spaces is as follows:

$$\boldsymbol{M}(\boldsymbol{r}) = \boldsymbol{M_s}\boldsymbol{m}(\boldsymbol{r}); \boldsymbol{m}\cdot\boldsymbol{m} = \mathbf{1} \tag{1-1}$$

Where $\boldsymbol{M_s}$ is the saturation magnetization intensity of the magnet. When the temperature is fixed and below the Curie temperature, $\boldsymbol{M_s}$ is a constant value. $\boldsymbol{m}$ is the normalized local magnetization vector, and all the energy items can be assembled together by $\boldsymbol{M}(\boldsymbol{r})$. The total energy in the system is expressed as:

$$\boldsymbol{E_{tot}} = \boldsymbol{E_{ex}} + \boldsymbol{E_{ani}} + \boldsymbol{E_{deg}} + \boldsymbol{E_{zeem}} + \boldsymbol{E_{dm}} \qquad \textbf{(1-2)}$$

$\boldsymbol{E_{ex}}$ is exchange energy, $\boldsymbol{E_{ani}}$ is anisotropy energy, $\boldsymbol{E_{deg}}$ is demagnetization energy, $\boldsymbol{E_{zeem}}$ is Zeeman energy, and $\boldsymbol{E_{dm}}$ is DMI energy. In the following chapters, we will discuss the five energies of appeal.

1. 1. 1 Exchange energy

A ferro-magnetic material is characterized by spontaneous magnetism. In classical electrodynamics, adjacent spins are advantageous to antiparallel alignment in energy. Material that aligns its magnetic moments in parallel is ferromagnetic. If the magnetic moments align in an antiparallel fashion, the material is antiferromagnetic.

However, the magnetic moments in ferromagnetic materials undergo what is called an exchange interaction. A consequence of this quantum mechanical effect is that adjacent spins align in parallel, leading to macroscopic magnetization configurations that are uniform.

Using the classical Heisenberg Hamiltonian of two adjacent spins as a starting point, we will arrive at the micromagnetic expression for the energy exchanged

$$E_{i,j} = -J\boldsymbol{S}_i \cdot \boldsymbol{S}_j \qquad (1\text{-}3)$$

Where $E_{i,j}$ is the exchange energy between two adjacent magnetic moments $\boldsymbol{S}_i$ and $\boldsymbol{S}_j$, and J is the exchange integral. If the total exchange energy of the system is zero when the magnetic moments are arranged in parallel, then when the angle φ_{ij} between the adjacent spins of atoms is small and close to zero, the total exchange energy of the system is approximately equal to

$$\varepsilon_{\mathrm{ex}} = 2JS^2\sum\left(1-\cos\,\varphi_{ij}\right) = 4JS^2\sum\sin^2\left(\frac{1}{2}\varphi_{ij}\right) \approx JS^2\sum\varphi_{ij}^2 \quad (1\text{-}4)$$

1. 1. 2 Anisotropy energy

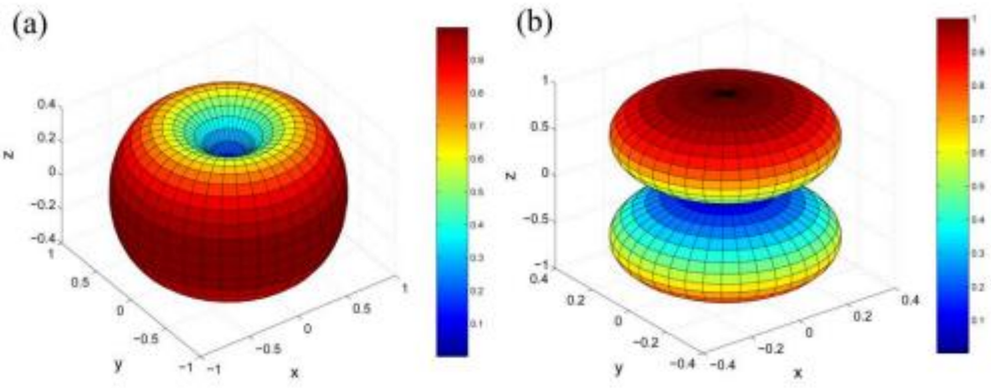

Figure 1.2 Uniaxial anisotropy energy density. (left) easy axis anisotropy ($K_1 > 0$). (right) easy plane anisotropy (($K_1 < 0$).[27]

Anisotropy is a dependence of energy level on some direction. In other words, ‘anisotropy’ means "directionally dependent". Magnetocrystalline anisotropy is one of the origin of magnetic anisotropic energy in magnetic materials [22]. This spontaneous orientation of atoms in ferromagnets is often called the "easy" orientation, meaning that the atoms is in the lowest energy state compare with other orientation. When studying magnetocrystalline anisotropy, current energy is applied to the magnetic system, the external fields drive the crystals to deflect from the "easy" plane to "hard" plane. Anisotropic energy is defined as the energy required to perform this operation. In other words, the magnetization energy required for magnetization along the hard and easy magnetization axes of ferromagnets differs, with the minimum magnetization energy required in the easy magnetization direction and the maximum required in the hard magnetization direction. The energy in the magnetic system is induced by the interaction between th e magnetic atoms and the crystal lattice of the material under study. Mostly, the materials with magnetically anisotropic energy have two lowest energy states directions to magnetize the material, with an angle as 180 degree. However, the magneto-crystalline anisotropy energy is defined as the energy consumed when the magnetization vector deflects from the easy axis, and its magnitude does not change with the reversal of the magnetization vector by 180 degrees. Therefore, the density of magnet crystal anisotropic energy surface is a function of direction cosine, which is defined as follows:

$$\varepsilon_{\mathrm{k}} = k_0 + \sum_i k_i \gamma_i^2 + \sum_i k_{2i} \gamma_i^4 + \sum_{i \neq j} k_{3ij} \gamma_i^2 \gamma_j^2 + \cdots \tag{1-5}$$

An example is hexagonal crystals, which are also known as uniaxial crystals. There are two easy magnetization directions for uniaxial crystals, and they are 180 degrees apart. Both of these directions of the magnetization curves and the anisotropic energy of magneto crystals are the same. If the Z axis is taken to be the main symmetry axis of the crystal, and angle θ between the direction of magnetization and the Z axis. The expression for the energy density of uniaxial anisotropy is

$$\varepsilon_{\mathrm{k}} = K_0 + K_1 \sin^2 \theta + K_2 \sin^4 \theta + K_3 \sin^6 \theta + \cdots \tag{1-6}$$

Where, K0, K1, K2, and K3 are uniaxial anisotropic constants. Due to the fact that K0 represents zero energy, K0 is of no practical significance and can be ignored. For higher-order terms, they can be ignored in most cases. Then formula 1-6 can be simplified as:

$$\varepsilon_{\mathrm{k}} = K_1 \sin^2 \theta \tag{1-7}$$

It is evident that the behavior of uniaxial anisotropy depends on the sign of K_1. Accordingly, when $K_1 > 0$, the energy density of uniaxial anisotropy has a minimum value in the case of $\theta = 0$ and π, so that the z axis represents the direction of the easy axis, as shown in Figure 1.2 (a). When $K_1 < 0$, The uniaxial anisotropic energy density has a minimum value when $\theta = \pi/2$, and, thus, the Z axis is in the direction of the hard axis, and the easy axis is located in any direction of the X-Y plane, as shown in figure 1.2 (b).

1. 1. 3 Zeeman energy

The Zeeman energy of a ferromagnetic body is the energy of the magnetization $\boldsymbol{M}$ in an external field $\boldsymbol{H}_{\mathrm{ext}}$ given by

$$\varepsilon_{\mathrm{zeem}} = -\mu_0 \boldsymbol{M} \cdot \boldsymbol{H}_{\mathrm{ext}} \tag{1-8}$$

Where μ_0 is the vacuum permeability. Thus, the total zeeman energy of magnetic materials is

$$E_{\mathrm{zeem}} = -\mu_0 \int \boldsymbol{M} \cdot \boldsymbol{H}_{\mathrm{ext}} \mathrm{d}V \tag{1-9}$$

Thus, the Zeeman can have its minimum when $\boldsymbol{M}$ is parallel to the direction of $\boldsymbol{H}_{\mathrm{ext}}$.

1. 1. 4 Energy of the demagnetizing field

A magnetized material's surface and inhomogeneous areas accumulate magnetic charges. Due to these magnetic charges, a magnetic field is produced in the opposite direction to the original magnetization. This magnetic field is known as the demagnetization field. The energy generated by the magnetization vector of the material itself in order to overcome the demagnetization field is called demagnetization energy, also known as stray field (outside the magnet). Determining the energy density of a demagnetization field is similar to the zeeman energy density, whose specific expression is as follows:

$$\varepsilon_{\mathrm{deg}} = -\mu_0 \boldsymbol{M} \cdot \boldsymbol{H}_{\mathrm{deg}}, \tag{1-10}$$

The demagnetization energy of magnetic materials can be obtained by integrating:

$$\varepsilon_{\mathrm{deg}} = -\mu_0 \boldsymbol{M} \cdot \boldsymbol{H}_{\mathrm{deg}} dV \tag{1-11}$$

The magnetic charge $\boldsymbol{H}_{\mathrm{deg}}$ originates from the bulk density and surface density of the magnetic field. The expression for $\boldsymbol{H}_{\mathrm{deg}}$ is:

$$H_{\mathrm{deg}} = -\frac{1}{4\pi}\left(-\int_V \nabla \cdot \boldsymbol{M}(\boldsymbol{r}') \frac{\boldsymbol{r}-\boldsymbol{r}'}{|\boldsymbol{r}-\boldsymbol{r}'|^3} \mathrm{d}^3 r' + \int_S \boldsymbol{n} \cdot \boldsymbol{M}(\boldsymbol{r}') \frac{\boldsymbol{r}-\boldsymbol{r}'}{|\boldsymbol{r}-\boldsymbol{r}'|^3} \mathrm{d}^2 r'\right), \tag{1-12}$$

Where $\boldsymbol{n}$ is the normal direction of the magnet surface.

1. 1. 5 Dzyaloshinskii-Moriya interaction energy

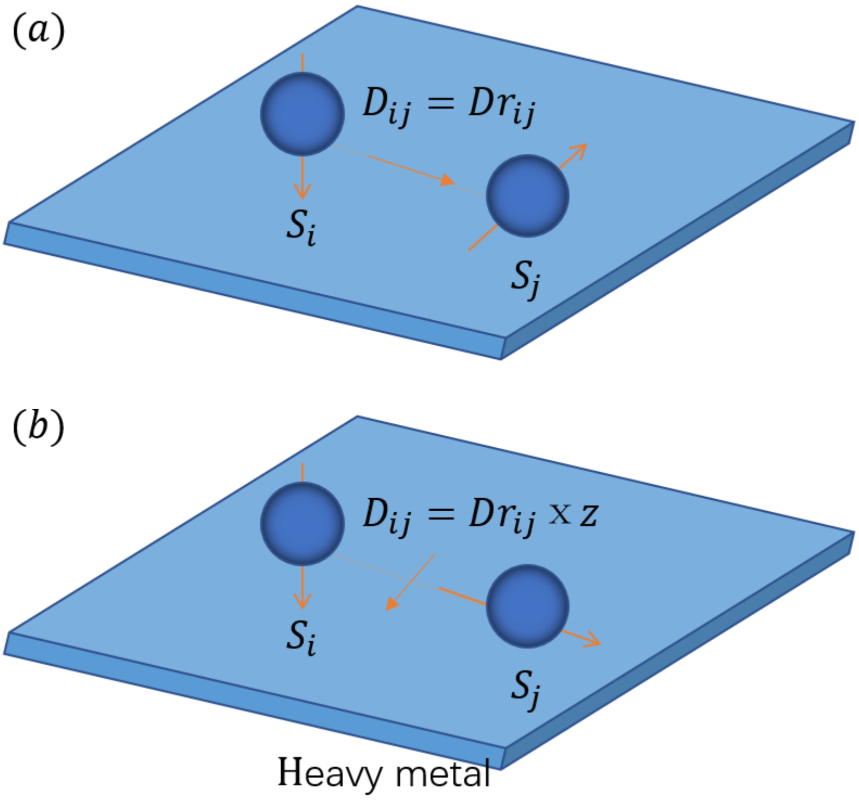

Figure 1.3 (a) Block DMI ,(b) Interface DMI

The Dzyaloshinskii-Moriya interaction (DMI) is an antisymmetric exchange interaction that stabilizes chiral spin textures. The expression of Hamiltonian is

$$H_{\mathrm{DM}} = -\boldsymbol{D}_{ij} \cdot \left(\boldsymbol{S}_i \times \boldsymbol{S}_j\right) \tag{1-13}$$

Where $\boldsymbol{D}_{ij}$ is vector of DMI, and $\boldsymbol{S}_i\, \boldsymbol{S}_j$ are two adjacent spins ions. Figure 1.3 (a) illustrates the block structure of DMI found in materials with lacking central symmetry of atomic structure, such as MnSi, FeCoSi and FeGe. The DMI vector $\mathbf{D}_{ij} \propto \mathbf{r}_i \times \mathbf{r}_j = \mathbf{r}_{ij} \times \mathbf{x}$, where D is the constant of DMI strength. Another type of DMI has been demonstrated to exist in magnetic films with broken interface geometric symmetry, usually at the junction of magnetic films and heavy metals , which call interface DMI. As shown in figure 1.3 (b), the DMI vector $\boldsymbol{D}_{ij} = Dr_{ij} \times z$. DMI may induce various types of topological magnetic structures in magnetic materials, such as chiral domain walls and skyrmion. At position r, the direction of magnetization is $m(r)$. Therefore, the energy expression for block DMI is as follows [28, 29]:

$$E_{\mathrm{BulkDMI}} = \iiint D\left[m_{\mathrm{y}}\frac{\partial m_{\mathrm{z}}}{\partial x} - m_{\mathrm{z}}\frac{\partial m_{\mathrm{y}}}{\partial x} + m_{\mathrm{z}}\frac{\partial m_{\mathrm{x}}}{\partial y} - m_{\mathrm{x}}\frac{\partial m_{\mathrm{z}}}{\partial y}\right]\mathrm{d}^3\boldsymbol{r} \tag{1-14}$$

The interface DMI energy is distributed evenly in the t thickness magnetic film, and therefore the interface DMI can be expressed as:

$$E_{\mathrm{InterDMI}} = t\iint D\left[m_{\mathrm{x}}\frac{\partial m_{\mathrm{z}}}{\partial x} - m_{\mathrm{z}}\frac{\partial m_{\mathrm{x}}}{\partial x} + m_{\mathrm{y}}\frac{\partial m_{\mathrm{z}}}{\partial y} - m_{\mathrm{z}}\frac{\partial m_{\mathrm{y}}}{\partial y}\right]\mathrm{d}^2\boldsymbol{r}. \tag{1-15}$$

1. 2 Gibbs free energy

When the Gibbs free energy of the entire system is at its minimum, the thermodynamic system reaches an equilibrium position.

The minimum value of free energy is obtained by a variational solution of the total energy of the system. When the magnetization vector in a ferromagnet is in equilibrium, its direction should be parallel to the total effective magnetic field. At this point, the moment acting on the magnetization vector is zero, and the expression of Brown's equation is as follows:

$$\frac{\partial \boldsymbol{E_{tot}}}{\partial \boldsymbol{m}} = \boldsymbol{m} \times \boldsymbol{H_{eff}} = \boldsymbol{0} \tag{1-16}$$

$\boldsymbol{H_{eff}}$ is the sum of effective magnetic fields, including exchange field $\boldsymbol{E_{ex}}$, anisotropic field $\boldsymbol{E_{ani}}$, demagnetization field $\boldsymbol{E_{deg}}$, Zeeman field $\boldsymbol{E_{zeem}}$ and DMI field $\boldsymbol{E_{dm}}$:

$$\boldsymbol{E_{eff}} = \boldsymbol{E_{ex}} + \boldsymbol{E_{ani}} + \boldsymbol{E_{deg}} + \boldsymbol{E_{zeem}} + \boldsymbol{E_{dm}} \tag{1-17}$$

The relationship between the total effective magnetic field and Gibbs free energy of the system is as follows:

$$\boldsymbol{H_{eff}} = -\frac{\boldsymbol{1}}{\boldsymbol{\mu_0 M_s}}\frac{\boldsymbol{\partial E_{tot}}}{\boldsymbol{\partial m}} \tag{1-18}$$

When the magnetization is parallel to the effective field, the system energy is the lowest.

1. 3 Dynamic micromagnetics

Even though Brown's equation provides a solution to the energetic equilibrium equation, some non-steady conditions, such as the application of a field pulse or an AC field, need to be solved by the Landau-Lifshitz-Gilbert equation.

1. 3. 1 Magnetization dynamics

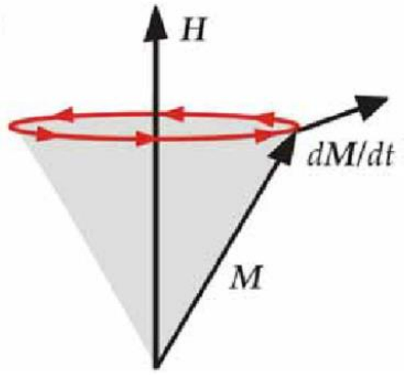

Figure 1.4 Magnetisation precession without damping.[30]

A ferromagnet derives its magnetism from the extranuclear electron, which includes an orbital magnetic moment and a spin magnetic moment. Since the magnetic moment of a nucleus is small, it can be ignored in the problems we consider. When $\boldsymbol{M}$ is the magnetization of an atom, $\boldsymbol{J}$ is the angular momentum, and the equation is as follows

$$\mu_0 \boldsymbol{M} = -\gamma \boldsymbol{J}, \tag{1-19}$$

where μ_0 is the vacuum permeability, γ is the spin magnetic ratio, for electrons:

$$\gamma = \frac{\mu_0 |e|}{2m_\mathrm{e}} g, g = 2 \tag{1-20}$$

In the total effective field $\boldsymbol{H_{eff}}$, the magnetization $\boldsymbol{M}$ will be affected by a torque as follows:

$$\boldsymbol{L} = \mu_0 \boldsymbol{M} \times \boldsymbol{H}_\mathrm{eff} \tag{1-21}$$

It is the change in angular momentum of the magnetization with time that is the torque. Therefore, we have:

$$\frac{\mathrm{d}\boldsymbol{J}}{\mathrm{d}t} = \boldsymbol{L} = \mu_0 \boldsymbol{M} \times \boldsymbol{H}_{\mathrm{eff}} \tag{1-22}$$

Substituting equation 2-22 into equation 2-20, then we can reach equation 1-23 after rearranging.

$$\frac{\mathrm{d}\boldsymbol{M}}{\mathrm{d}t} = -\gamma \boldsymbol{M} \times \boldsymbol{H}_{\mathrm{eff}} \tag{1-23}$$

Equation 1-23 represents magnetisation precession without damping. According to figure 1.4, when a vertical upward effective field $\boldsymbol{H}_{\mathrm{eff}}$ is applied to magnetization $\boldsymbol{M}$, and the vector of magnetization $\boldsymbol{M}$ performs a continuous circular motion around $-\boldsymbol{M} \times \boldsymbol{H}_{\mathrm{eff}}$. It is the magnetization precession for undamped motion.

1. 3. 2 Magnetization dynamics with damping

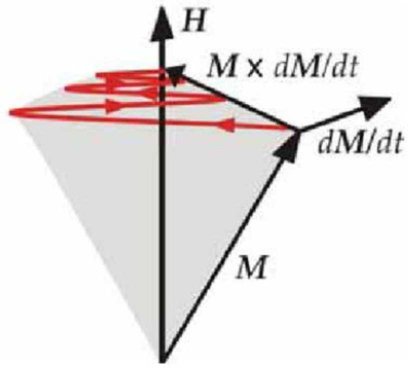

Figure 1.5 Magnetisation precession with damping.[30]

The equation 1-23 could be used only in a case of small damping. The strong damping in thin films also causes a damping torque that pulls $\boldsymbol{M}$ towards $\boldsymbol{H}_{\mathrm{eff}}$ as it precesses around $\boldsymbol{H}_{\mathrm{eff}}$. In this case, we need to add the damping term $\boldsymbol{T_D}$ to the right-hand side of the equation 1-23. Therefore, we have:

$$\frac{\mathrm{d}\boldsymbol{M}}{\mathrm{d}t} = -\gamma \boldsymbol{M} \times \boldsymbol{H_{eff}} + \boldsymbol{T_D} \tag{1-24}$$

There are three forms of expression for the damping term. First, there is Landau-Lifshitz damping form[31], which is as follows:

$$\boldsymbol{T}_{\mathrm{D}} = -\frac{\alpha\gamma}{M_{\mathrm{s}}} \boldsymbol{M} \times (\boldsymbol{M} \times \boldsymbol{H}_{\mathrm{eff}}) \tag{1-25}$$

Where α is a dimensionless constant called the damping factor, represents the rate of magnetization $\boldsymbol{M}$ to $\boldsymbol{H_{eff}}$. And M_s is the saturation magnetization. The second is Bloch damping form[32], which is described as follows:

$$\boldsymbol{T}_{\mathrm{D}} = -\frac{1}{T}(\boldsymbol{M} - \chi_0 \boldsymbol{H}_{\mathrm{eff}}) \tag{1-26}$$

Where T is represent relaxation times, and χ_0 is longitudinal susceptibility. The third is Gilbert damping form[33], which is described as follows:

$$\boldsymbol{T}_{\mathrm{D}} = \frac{\alpha}{M_s}\left(\boldsymbol{M} \times \frac{\mathrm{d}\boldsymbol{M}}{\mathrm{d}t}\right) \tag{1-27}$$

As mentioned above, all three types of damping terms are equivalent, but since the Gilbert form is more convenient in application and generalization than the other two kinds, we now use the Gilbert form for damping terms. Landau-Lifshitz-Gilbert (LLG) equation is expressed as follows:

$$\frac{\mathrm{d}\boldsymbol{M}}{\mathrm{d}t} = -\gamma \boldsymbol{M} \times \boldsymbol{H}_{\mathrm{eff}} + \frac{\alpha}{M_s}\left(\boldsymbol{M} \times \frac{\mathrm{d}\boldsymbol{M}}{\mathrm{d}t}\right) \tag{1-28}$$

Figure 1.5, is subject to two torques: one is $-\boldsymbol{M} \times \boldsymbol{H}_{\mathrm{eff}}$, which causes $\boldsymbol{M}$ to rotate in a circle around $\boldsymbol{H}_{\mathrm{eff}}$; another is $\boldsymbol{M} \times \frac{\mathrm{d}\boldsymbol{M}}{\mathrm{d}t}$, which tends $\boldsymbol{M}$ towards the direction of the effective field $\boldsymbol{H}_{\mathrm{eff}}$. In the combined action of the two torques, the arrow's trajectory of $\boldsymbol{M}$ no longer resembles a circle, but rather a spiral that gradually leans toward $\boldsymbol{H}_{\mathrm{eff}}$. In 1996, Slonczewski extended the model to include spin-transfer torque, i.e. torque generated by spin-polarized current flowing through the ferromagnet during magnetization. Commonly, this expression is written as $m = \boldsymbol{M}/\boldsymbol{M_s}$:

$$\frac{\mathrm{d}\boldsymbol{m}}{\mathrm{d}t} = -\gamma \boldsymbol{m} \times \boldsymbol{H}_{\mathrm{eff}} + \alpha \boldsymbol{m} \times \frac{\mathrm{d}\boldsymbol{m}}{\mathrm{d}t} \tag{1-29}$$

1. 4 Magnetic skyrmion

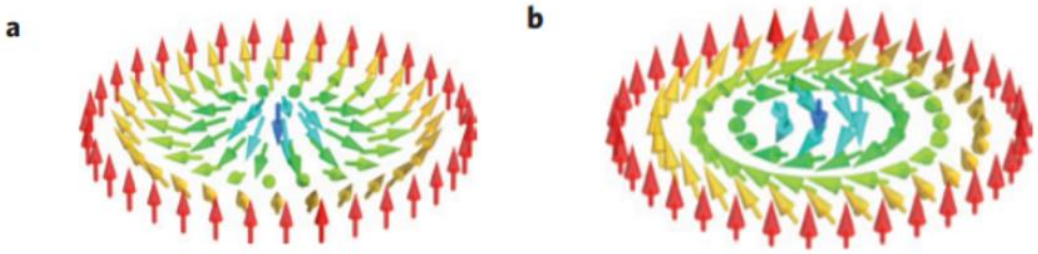

Figure 1.6 Two types of magnetic skyrmions[34] :(a) Bloch skyrmion; (b) Neel skyrmion

In condensed matter systems, magnetic skyrmions have been observed experimentally and predicted theoretically. As well as in bulk magnetic materials such as MnSi, skyrmions can also be formed in thin magnetic films. It is possible for skyrmions to be achiral, or chiral (figure 1.5 a and b are both chiral skyrmions) in nature, and to exist both as dynamic excitations or as stable or metastable states. Even though the broad contours of magnetic skyrmions have been established de facto, a variety of ideological interpretations exist with slight variations.

1. 4. 1 Definition of skyrmion

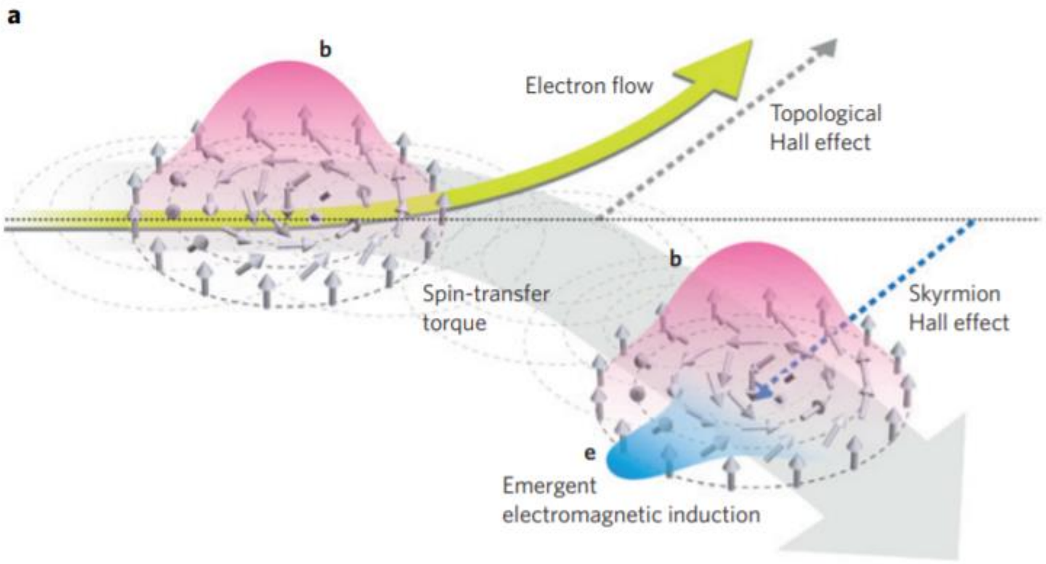

Figure 1.7 Motion of skyrmions driven by an applied current and the topological Hall effect (THE).[35]

The skyrmions are vector fields with a spherical topology characterized by topological charges. It is usually referred to as a skyrmion number, which can be expressed mathematically as

$$n = \frac{1}{4\pi}\int \mathbf{M} \cdot \left(\frac{\partial \mathbf{M}}{\partial x} \times \frac{\partial \mathbf{M}}{\partial y}\right) dxdy \tag{1-30}$$

Where n is the skyrmion number, which is the number of times spins wind around the unit sphere. The unit vector $\mathbf{M}$ indicates the direction of the local magnetization within the magnetic thin, and the integral is taken over a two-dimensional space. Alternatively, one can obtain n by wrapping the spin unit vector $\mathbf{M}$ around a unit sphere, then $n = 1$. By determining structure stability, which is the subject of this thesis, this concept remains valid for magnetic skyrmions and bimerons.

1. 4. 2 Skyrmion nucleation

As skyrmion structures are topologically protected, the barrier of topological stability needs to be overcome in the process of nucleation [36]. There are a number of means to achieve this objective, including external magnetic fields, local thermal effects, Dipole-dipole interaction, Dzyaloshinskii-Moriya interaction, etc. If the external magnetic field and temperature of the system are in an A-phase, then the spin distribution in the structural material system of material B20 (MnSi, FeGe, etc.) produces an energy ground state composed of skyrmion[1, 37]. Nevertheless, the resulting skyrmions will first nucleate at defects[38] or edges[39] in the material. It is true that external means such as magnetic fields and lasers have been used to overcome these problems, however, they are not applicable to our simulation of skyrmions. Compared to skyrmions by DMI, skyrmions are much larger (10^2). In the Dzyaloshinskii-Moriya interaction, neighboring spins are chiral-interacted so that a skyrmion lattice is nucleated in the presence of a magnetic field. For calculation of the quantity of a system with a length of a micrometer or greater, a large amount of CPU will be required. Consequently, the DMI type skyrmion with a scale of nanometer is the focus of the computational research presented.

1. 5 Numerical analysis

Micromagnetism uses the Finite Difference Method (FDM) or Finite Element Method (FEM) to separate a continuum into approximating the discrete elements by replacing the derivatives in the equation with differential quotients. The finite difference method is easy to implement but exhibits deviations when applied to irregular systems. Although the finite element method is suitable for all kinds of systems, it can be complicated in some irregular areas and requires strict continuity of the area to be considered. For both cases, the basic assumption is that the magnetization is constant, as illustrated in formula 1-1. Thus, the total energy of the system can be determined from formula 1-2, and the corresponding effective field from formula 1-14.

1. 5. 1 Finite difference method

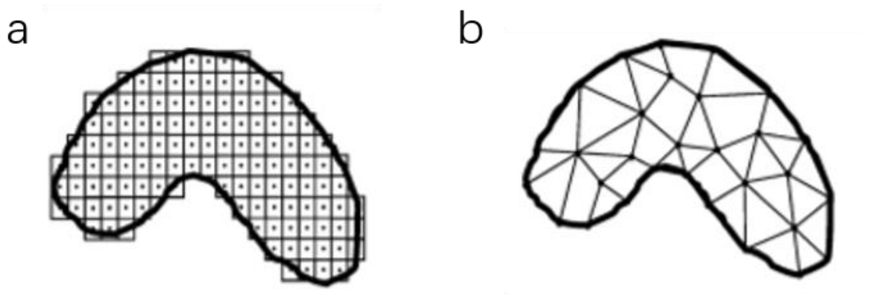

Figure 1.8 (a) A schematic diagram of FDM mesh pattern of domain. (b) A schematic diagram of FEM mesh pattern of domain.[40]

As shown in figure 1.8 (a), the finite-difference method always divides the simulated system into cuboids. Instead of continuous regions, finite cuboids are used, and the spatial derivative at each point is approximated by the difference quotient of the cuboids. In general, the differential equation solution is transformed into the solution of the cuboid field value difference equations, hence the name "finite difference method.". On the basis of whether the scheme is discrete in time, it can be classified as semi-discrete or fully discrete. It can be used to obtain different accurate approximations for the derivatives: first-order, second-order, and higher-order. At present, the Taylor series is commonly used to construct the difference. For systems with a regular magnetic structure, the finite difference method is applicable. As a result of the irregular system or the presence of a surface, the rectangular partition element is approximated with a step shape at the boundary or surface, resulting in a deviation in the calculation of the demagnetization field. The deviation can be corrected by adopting the boundary numerical method. Based on the method of calculation, it can be divided into two discrete methods: energy and field. By using the discrete method based on energy, the energy value can be calculated accurately by $\boldsymbol{m}(\boldsymbol{r})$, while the effective field represents the average value for the partition element. With the field-based discrete method, the effective field value is accurately calculated by $\boldsymbol{m}(\boldsymbol{r})$ and the energy is an incidental result.

1. 5. 2 Finite element method

As shown in figure 1.8 (b), the finite element method divides a complex structure into non-overlapping polyhedral elements, such as triangular, tetrahedra in 3-D or higher-order simplexes in multidimensional spaces. Taking nodes as the point of solving the difference, the related variables are replaced by an expression corresponding to the nodes within each element and the corresponding difference within the partition element, and the partial differential equation is constructed by utilizing the variational methods and weight functions. Since the subdivision element of finite element is a polyhedron structure, in a more complex system, a relatively smooth boundary can also be obtained, resulting in higher accuracy in the calculation of demagnetization energy. For this reason, the finite element method is more accurate than the finite difference method when dealing with complex systems. Although, the calculation speed of the finite difference method is slower than that of the subdivision at the boundary due to the refinement of the subdivision.

1. 5. 3 Mumax3

The Mumax3 software, developed by Arne Vansteenkiste and colleagues at the Ghent University in Belgium[23], is an open-source micromagnetic simulation program. As Mumax3's source code is written in Golang and CUDA, the software is dependent on NVIDIA CPUs for computation. It is currently available for Linux, Windows, and Mac, and updates quickly and frequently. In addition to being based on the same finite-difference method as OOMMF, MUMAX3 is 100 times faster for large-scale systems compared with CPU-based OOMMF, which is the primary reason for its popularity. Furthermore, the input script is in MUMAX3 format and the code is relatively simple.

1. 5. 4 Summary

The purpose of this chapter is to introduce the history of skyrmion and bimeron, as well as the fundamental physical principles of magnetic systems, such as Heisenberg Hamiltonian for static micromagnetism and LLG equation for dynamic micromagnetism. A description of the MUMAX3 calculation method and of its theoretical basis is given. Furthermore, the meanings and uses of skyrmion and bimeron are discussed, followed by the introduction of the basic features of magnetic skyrmion and bimeron. The next chapter will be devoted to discussing the thermal stability of skyrmion and bimeron.

Chapter.2 Effects of thermal effects on bimeron topology and comparison with skyrmion

The concept of micromagnetism is based on a continuum approximation of exchange interactions, including boundary conditions, and on Maxwell's equations of motion in the static limit. The total micromagnetic energy is the sum of exchange energy, anisotropy energy, Zeeman energy, demagnetization energy, and DMI energy. The properties of micromagnetism can be accurately described by a time-evolution equation, such as field-induced magnetization precession or damping when applied in space and time. With mathematical micromagnetism, it is possible to study the complexity of magnetic bodies of small sizes, such as calculating the topological charge numbers. Unfortunately, there are generally fewer calculation methods available. The topological charge number of skyrmion and bimeron is calculated using the finite-difference derivative method and lattice-based finite difference method in this study. The skyrmion and bimeron in magnetic materials can be characterised by a skyrmion number, which follows from the topological invariant. The skyrmion number can be written as: $Q = \frac{1}{4\pi}\int d^2rS \cdot (\partial_x S \times \partial_y S)$. The equation is only valid under the continuum condition, in which the spins in the system are almost parallel with their neighbours.

The results calculated using these two discretization methods are compared, so that the most appropriate scheme may be selected for calculating the topological charge number of thermal effects. A finite-difference method was proposed by Miltat and Donahue in 2007 to describe exchange interactions, boundary conditions, and demagnetization evaluation, and to monitor the time integrals[41]. Methods based on field data and energy data are described respectively. Under boundary conditions, the field-based method can be used to solve the LLG equation by directly identifying the effective field components. The energy density only works in this method if the effective field is a gradient of the energy density. Using the energy-based method, the magnetic energy calculated by discrete magnetization is primary, while the effective field is calculated from the total energy. The unit mean field is obtained with this method, and the equilibrium magnetization mode can be found directly by minimizing the energy. Even though this method is simpler and energy as an integral component is smaller and easier to approximate than changes in the field, it does not reflect variations in the demagnetization along the normal direction of the film. Moreover, they failed to account for disorders such as thermal effects, which can affect the accuracy of cells. In 2020, Joo-von Kim and Jeroen Mulkers proposed an implementation of finite-difference micromagnetism[42]. It is a lattice-based approach based on B Berg and M Luscher's work[43]. To verify the implementation, three examples are provided: An isolated skyrmion with periodic boundary conditions, soliton pair generation in the ferromagnetic orbit, and an isolated skyrmion in a constrained structure at finite temperature. This article discusses that the finite difference method based on the lattice can well remedy the false change of topological charge owing to the inaccurate finite difference derivative, and the calculated topological number can well quantify the process of skyrmion nucleation and annihilation. Since the topological charge is often substituted for the gradient of magnetization in the annihilation process, it remains impossible to describe the gradient of magnetization of skyrmion.

2. 1 Finite difference methods and lattice-based implementation

A ferromagnetic state or a trivial state is determined by topological charge Q, which describes the internal winding number of the classical spin ($\Pi_2(S^2)$ homotopy group)[44, 45] of 2+1 dimensions. Skyrmions contribute to the topological charge in the universe by contributing ±1 to it. The formula 2-1 is used to compute topological charge Q in general. Through topological charge Q there is also a possibility of determining whether skyrmion or bimeron exist in the sample on the basis of topological charge Q.

$$Q = \frac{1}{4\pi} \int d^2 x \mathbf{m} \cdot \left(\frac{\partial \mathbf{m}}{\partial x} \times \frac{\partial \mathbf{m}}{\partial y} \right) \tag{2-1}$$

An application of this quantity is to describe the topology of the spin structure in a two-dimensional system, for example e.g.,[46], where **m** represents the direction of the magnetic moment. The number of torques around the unit sphere is measured by Q when $M(r)$ is projected onto it. In vortices and merons, Q equals 1/2, and in skyrmions, Q equals 1. For numerical micromagnetism, one of the most commonly used methods is to discretize $M(r,t)$ using finite difference methods[23, 41]. Based on this assumption, the energy exchange in **m** between the two cells (approximately equal to the lowest order $(\nabla \mathrm{m})^2$) makes sense.

When **m** varies greatly in space, problems occur, such as in nucleation and annihilation of vortices and storms, or in stochastic dynamics with random fields, which leads to inaccurate values of Q. Figure 2.1(a)(b) depicts the equilibrium profile calculated with the parameters in MUMAX3 codes [4] and [5], showing skyrmion and bimeron at 0K. Eq. (2-1) gives the $Q_{skyrmion} = -1.0026203$ and $Q_{bimeron} = -1.0001248$ Qbimeron= of this configuration, which is close to the theoretical value Q =−1, which is acceptable. Considering the effects of disorder, such as caused by thermal fluctuations, in figure 2.1(a), each torque randomly deviates from its equilibrium orientation, as shown in figure 2.1. (c). Figure 2.1(c)(d) illustrates the corresponding distribution of this disorder on the unit sphere. Despite the distortion in the mesh, it retains the same topology as in figure 2.1(b)(d) and thus retains the same charge. The values of $Q_{skyrmion} = -0.99686474$ and $Q_{bimeron} = -0.93721527$ given in equation (2-1) are indicative of the loss of precision of finite difference derivatives. The thermal effect in the system is considered as a random distribution effective field which will influence the effective magnetic properties.

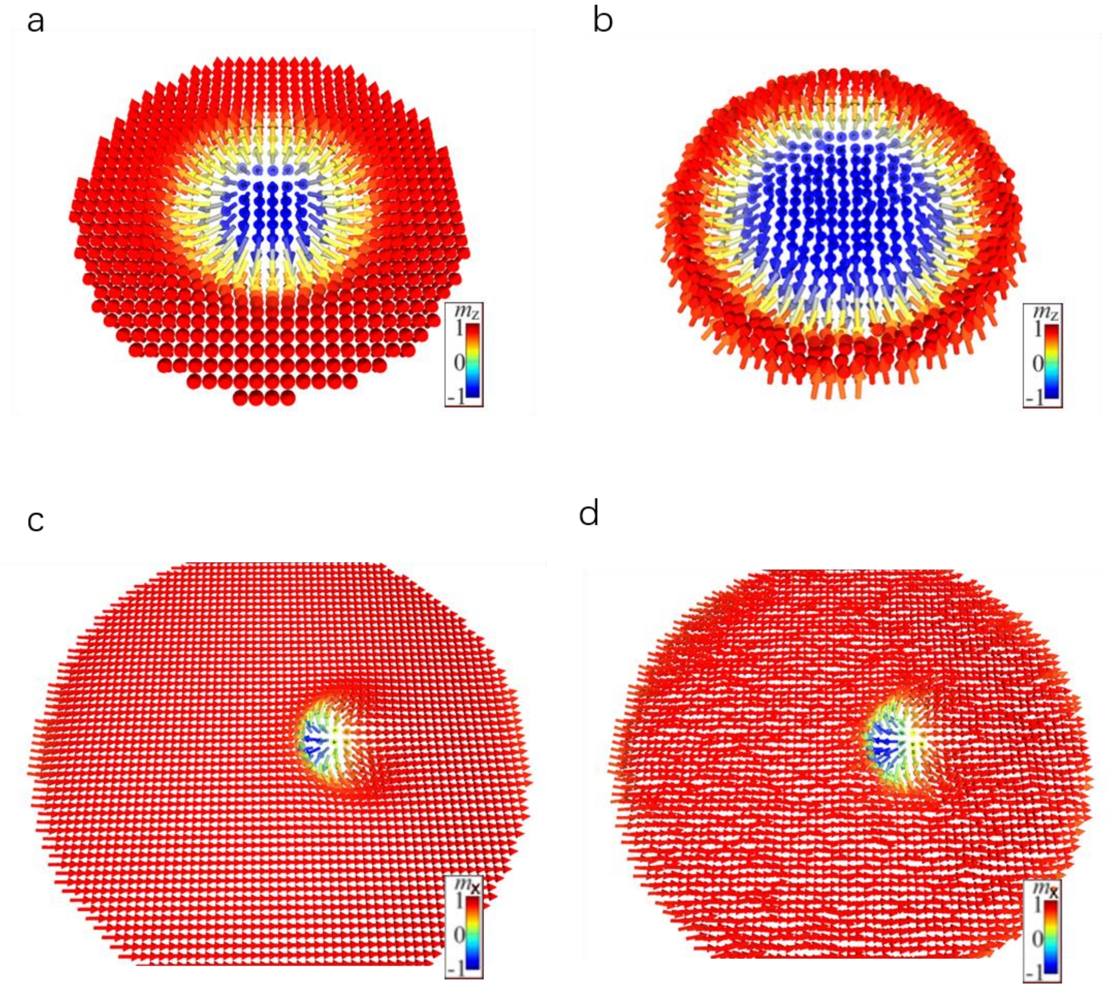

Figure 2.1 (a) Projection of skyrmion structure in a 2d plane at zero temperature. (b) An example of a disordered m_z of skyrmion at a finite temperature. (c) Projections of bimeron structures on two-dimensional surfaces at zero temperature. (d) Examples of disordered bimeron m_z at finite temperatures.

Berg and Luscher derived the explicit expression for the topological charge of the lattice spin field [43], which has been applied in atomic spin dynamics and Monte Carlo simulations[47, 48]. The three moments in figure 2.2(a) represents the average magnetization direction of the finite difference element. These moments are viewed as lattice spins, and the interactions between them are ignored. Figure 2.2(a) illustrates the average magnetization orientation in a finite-difference cell. On the unit sphere, the topological charge is given by the sum of the set of elementary triangles,

$$Q = \frac{1}{4\pi} \sum_{\langle uvw \rangle} q_{uvw} \tag{2-2}$$

Where

$$\tan\left(\frac{q_{uvw}}{2}\right) = \frac{\mathbf{m}_u \cdot (\mathbf{m}_v \times \mathbf{m}_w)}{1 + \mathbf{m}_u \cdot \mathbf{m}_v + \mathbf{m}_u \cdot \mathbf{m}_w + \mathbf{m}_v \cdot \mathbf{m}_w} \quad (2\text{-}3).$$

Here, it's constant under the exponential uvw cycle. Figure 2.2(a) shows the two signed triangles that make up the cell, q_{124} (gray) and q_{234} (white). Figure 2.2(b) represents another equally valid definition (uvw) equation (2-2) indicating that the sum is limited to the unique triangle shown in figure 2.2(a) or 2.2(b).

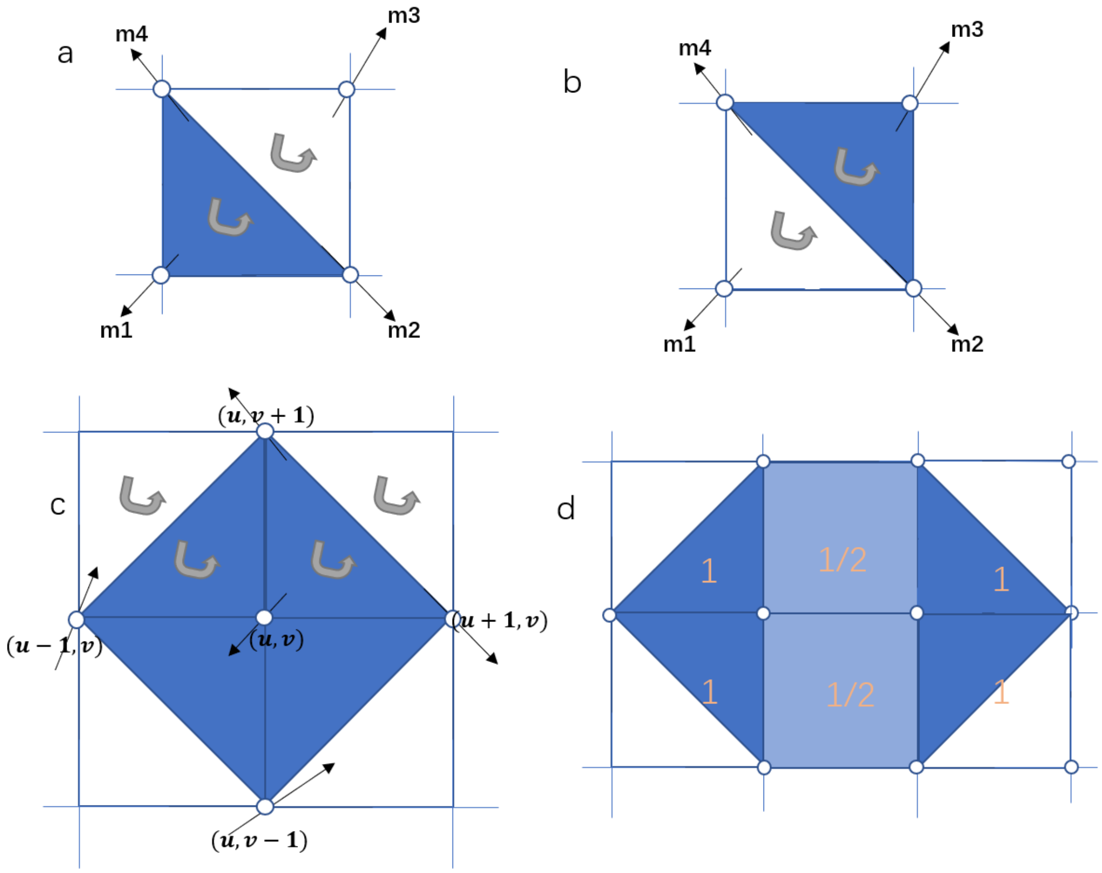

Figure 2.2 Calculate the topological charges by using the lattice scheme. (a) The cell is comprised of two signed triangles, q_{124} *and* q_{234}*. (b) An alternative definition of a signed triangle. (c) An algorithm for calculating the local charge density at a site (u, v) by averaging the two cells intersected by a triangle formed by the nearest neighbor. (d) Scheme for an arbitrary finite-size geometry, where the number corresponds to the weight and the cross corresponds to the vacant spaces.*

As shown in figure 2.2(c), a variation of this scheme may be employed in order to define a local charge density similar to equation (2-1) at a site (u,v) associated with the coordinates of the finite difference element defining $\boldsymbol{m}_{uv}$. It consists of four triangles spanned by (u,v) and their neighboring spins (u + 1,v), (u,v + 1), (u - 1,j) and (u,v - 1), each of which has at least two unit cells. This method uses two conventions in figure 2.2 (a) and (b), and averages the two, thereby allocating 1/2 of the weight of each triangle $\boldsymbol{q}_{uvw}$. With a system of limited size, the same average process cannot be applied to the curve boundary edge because there are only three defined triangles, for example, in figure 2.2 (d) of the upper left and lower right blue triangles. Weights are assigned to isolated signed triangles in this case.

2. 2 Simulation skyrmion and bimeron examples with the lattice-based approach

For the isolated ferromagnetic skyrmions in the $120 \times 120 \times 0.6\ nm$ film, the film plane is separated by a $120 \times 120 \times 1\ \ nm$ finite difference element and has periodic boundary conditions. We use an exchange constant $A = 15pJm^{-1}$, saturation magnetization $M_s = 47e\text{^}4\ A/m$, A vertical magnetic anisotropy constant $Ku = 0.6e\text{^}6\ j/m^3$, and an interfacial Dzyaloshinskii-Moriya interaction (DMI) constant $D = 0.6e\text{^}6\ j/m^2$, gilbert damping αlpha= 0.05. The demagnetization enerigy is included in the simulations. Figure 2.3 shows the evolution of Q(t) above 10ns at three different temperatures, in which the adaptive time-step integration method is used to solve the Landau Lifshitz equation [13]. In MUMAX3, the topological number is calculated at 0.2ns intervals, using finite-difference derivatives (Equation 2-2). Q(t) calculated using finite difference derivatives fluctuates greatly, and its distribution expands with an increase in temperature, as illustrated by the histogram in figure 2. 3. Consequently, the resulting time average Q coincides with the peak value of the distribution function P(Q), but does not coincide with the expected value of -1. The lattice-based approach, on the other hand, gives a near-constant Q over temperature and simulation time ranges, where the fluctuation (invisible) is mainly related to the limitations of the single-precision floating-point algorithm (e.g., Q = -1.0000001, -1.0000004, -1.0000008, -1.0000002, And -0.9999996 at T = 400 K). At 80 K, the bias of Q = 1 can be detected by lattice-based method, where the transient 1/2 and 1 states are also shown in figure 2.3. They represent nucleation and annihilation of thermally driven pion states and isolated pion states respectively.

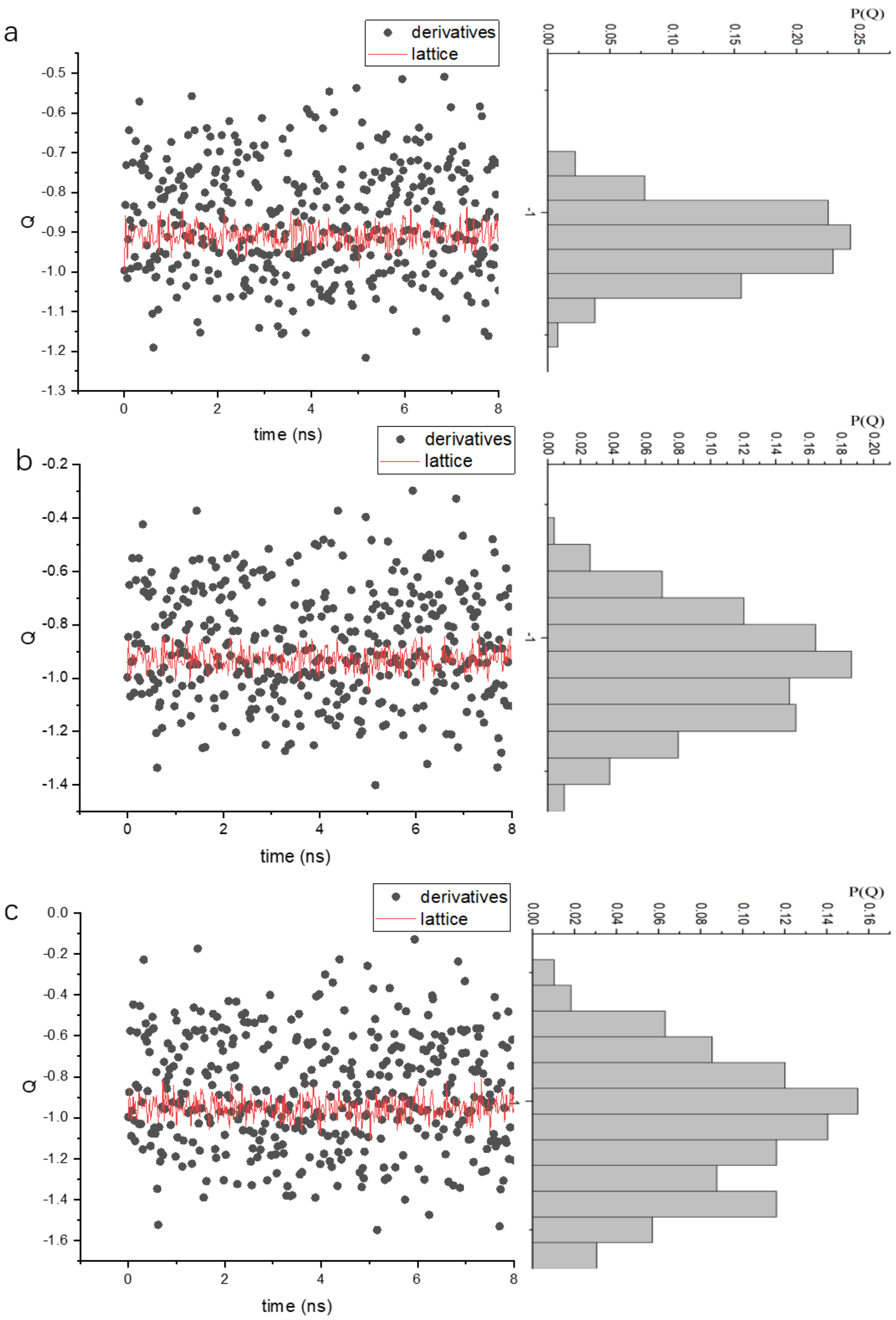

Figure 2.3 Compare Q(time) calculated with (1)(' derivative ') and (2)(3)(' lattice ') at skyrmion (a) 40 K, (b) 60 K, and (c) 80 K at different temperatures. The figure on the right is the probability density functions of Q obtained by formula (1).

Figure 2.4 studies the isolated ferromagnetic bimeron in a $120 \times 120 \times 1\ nm$ film. The sample, is discrete by a $120 \times 120 \times 1\ nm$ finite-difference element. Exchange constant $A = 15pJm^{-1}$, saturation magnetization $M_s = 47e\string^4\ A/m$, A vertical magnetic anisotropy constant $Ku = 0.6e\string^6\ J/m^3$, an interfacial Dzyaloshinskii-Moriya interaction (DMI) constant $D = 0.6e\string^6\ j/m^2$, gilbert damped αlpha= 0.05, the three different temperatures are 20K, 40K and 80K respectively, which are the same as skyrmion above. As shown in figure 2.4, finite-difference derivatives (Equation (2-1)) and latel-based method(Equation (2-2) (2-3)) have a large gap, Finite-difference derivatives are generally smaller than latel-based method. Moreover, Q fluctuates less under finite-difference derivatives method, mainly concentrated near the peak value, but it is more discrete. In the latel-based method, the particles are concentrated near Q=-1, indicating that the particles have a certain thermal stability in the current environment.

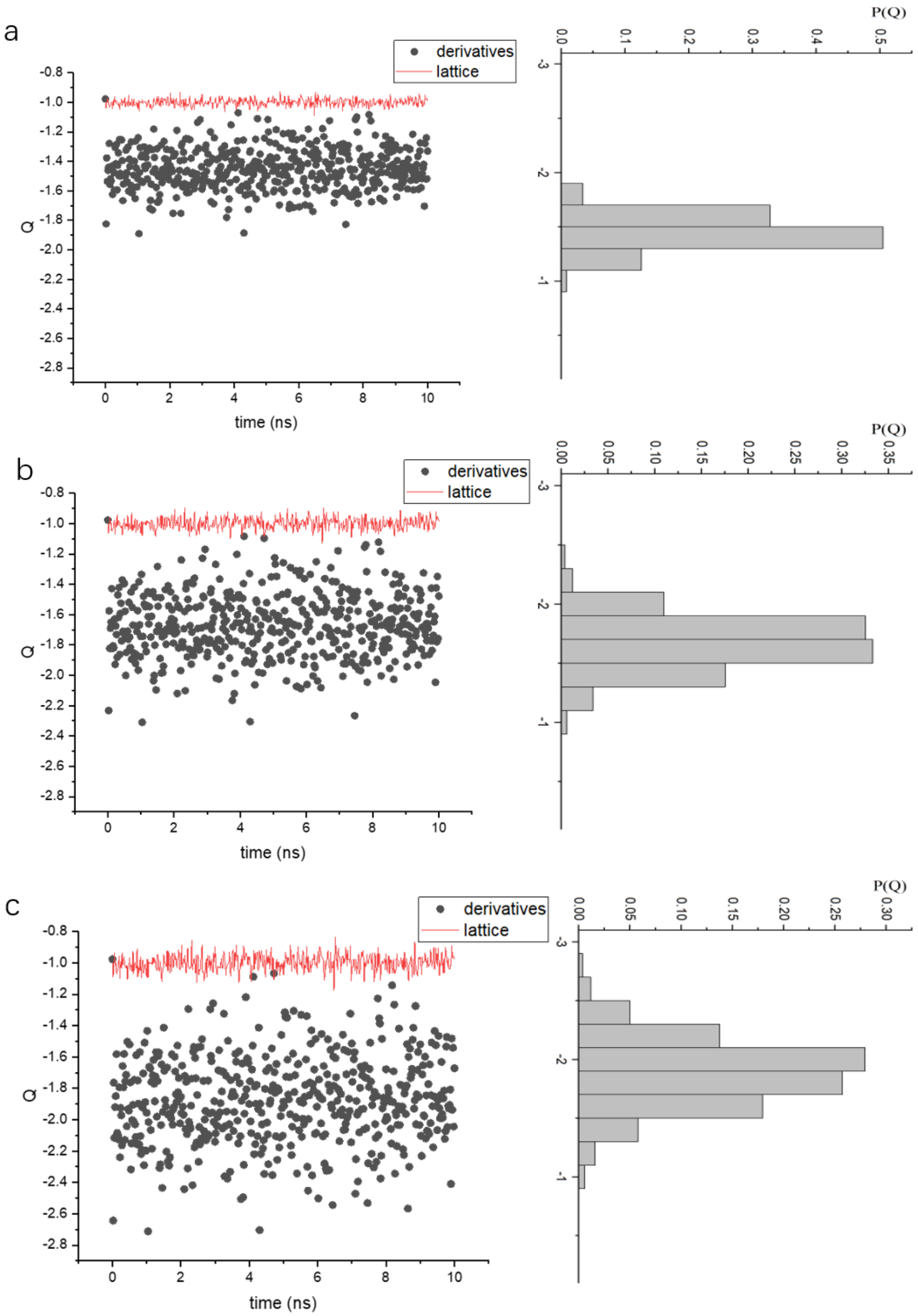

Figure 2.4 Compare Q (time) calculated using (1)(' derivative ') and (2)(3)(' lattice ') at bimeron(a) 40 K, (b) 60 K, and (c) 80 K at different temperatures. The figure on the right is the probability density functions of Q obtained by formula (1).

2. 3 Simulation bimeron domain and annihilation examples with the lattice-based approach

In this chapter, we examine the effect of the magnetic domain of a bimeron and its annihilation on Q values. The conversion between skyrmion and domain walls has been shown to be reversible, and bimeron, which is a topology of skyrmion, is also convertible with domain walls. The change of the bimeron Q from -1 to 0 signifies that the bimeron in the sample has become a domain wall or annihilation. Moreover, we are able to adjust the temperature to observe the bimeron Q changes in order to determine the bimeron status. By adjusting the temperature under identical conditions, however, the thermal stability of particles can be better compared. In figure 2.5, the transition between the bimeron and the domain walls is illustrated, while figure (a) illustrates the instantaneous change in Q. Figure 2.5(b) shows that Q=-1.0140985 is near -1, suggesting that the current bimeron topology is preserved. Based on figure 2.5(c), Q at this point is between -0.44121385 and -0.7069561, representing annihilation of meron. In the end, under the influence of the thermal effect, it becomes figure (d), completely transformed into magnetic domain walls.

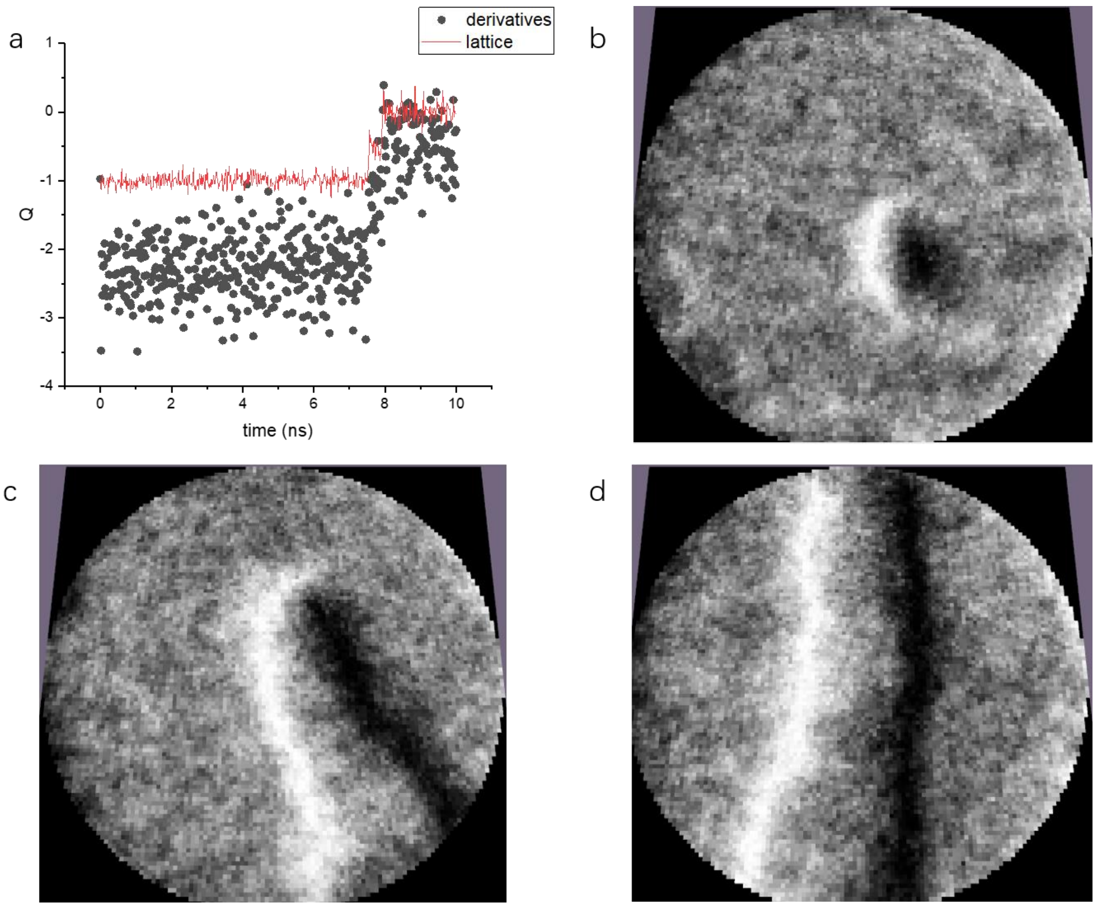

Figure 2.5 (a) Changes in instantaneous Q values, Figure (b)- Figure (d), bimeron conversion into domain walls. Here Ms = 470 kA/m, A=15pJ/m, D=4.2e^-3J/m^2, Ku=0.6e^6J/m^3, T=120K. (b) t=7.2ns, (c) t=7.56ns, (d) t=8ns.

Figure 2.6 depicts the bimeron annihilation process, while figure 2.6(a) depicts the instantaneous change in Q values. In this case, Q=-0.93794507, as illustrated in figure 2.6(b), indicates that the current bimeron topology still exists. At this point, Q equals -0.98566586, which has not yet begun annihilation, as shown in figure 2.6(c). Figure 2.6(d) represents the annihilation of meron as Q=-0.032889273 close to 0. The distribution of finite difference derivatives also represents the bimeron change process, but the deviation caused by the thermal effect is too large, so the bimeron's state change cannot be accurately quantified.

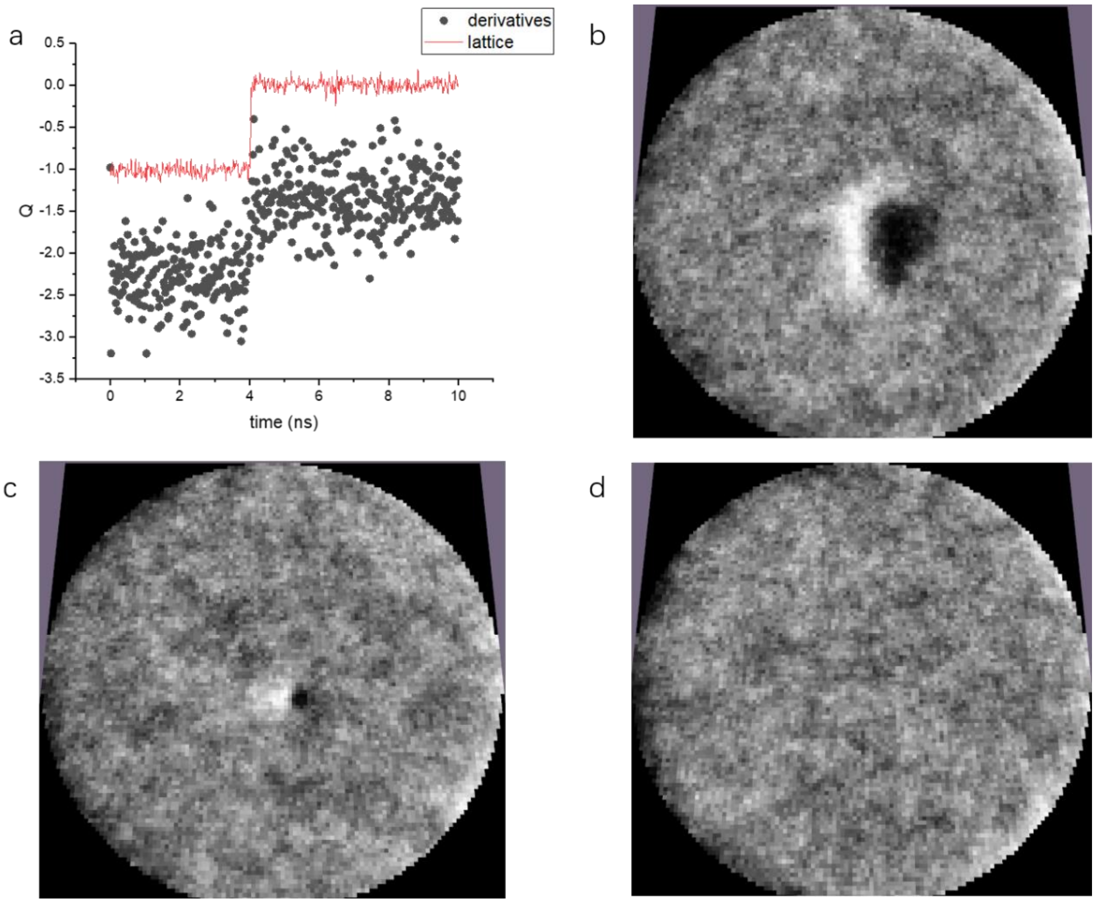

Figure 2.6 (a) Changes in instantaneous Q values, Figure (b)- Figure (d), bimeron annihilation process. Here Ms = 470 kA/m, A=15pJ/m, D=4.75e^-3J/m^2, Ku=0.8e^6J/m^3, T=100K. (b) t=3.98ns, (c) t=4.02ns, (d) t=8ns.

2. 3. 3 Summary

Our study of the stability of the skyrmion and bimeron has demonstrated that the inaccuracy of limited difference derivatives, especially in thermodynamic settings, can be resolved by using lattice-based methods which can be obtained through the MUMAX3 electromagnetic code. The use of lattice-based approaches does highlight the interpretation of nonintegral values for Q(t), especially when processes such as annihilation and thermal fluctuations are at work.

Chapter.3 Brownian motion comparison between skyrmion and bimeron under thermal effect

Brownian motion of non-interacting particles has been observed in a variety of scientific situations, including molecules suspended in liquids, optically captured microspheres, and spin structures in magnetic materials. For thermally stable spintronic devices, the study of spin texture Brownian motion is crucial. The experimental group of Yan Zhou and Wanjun Jiang et al. published a study in 2020 on isolated topologically dependent Brownian gyromotion[22]. In an asymmetric Ta/CoFeB/TaOx multilayer, the thermal wave-induced random walks of a single Néel-type magnet were observed experimentally by means of a polar magneto-optical Kerr effect (MOKE) microscope with both time and spatial resolution. Using the stochastic Thiele equation, a Brownian rotation motion with temperature-dependent diffusion coefficients and topologically dependent rotation motion is derived for a single skyrmion. Our research has been greatly benefited by the simulation of single skyrmion Brownian gyromotion. Thermal fluctuations affect spin forces in magnetic materials, especially when the magnetic anisotropic energy is equal to the thermal excitation. From the time-varying trajectory of skyrmion driven by thermal fluctuations, the random walk characteristics of skyrmion are revealed by introducing a stochastic Gaussian random wave field and using the Landau-Lifshitz-Gilbert equation (LLG). Lastly, it is shown that the trajectory amplitude increases with temperature, indicating a heat-induced diffusion. Brownian motion predicts this behavior. Essentially, as temperature increases, the size of the skyrmion grows, causing interaction and dissipation between it and the edge. A study by Y Yao, X Chen, and colleagues (2020) are also practical[49]. Known as TRNG (True Random Number Generators), they are built using continuous thermal Brownian motion. Initially, the behavior of the TRNG based on skyrmion is verified by micro-magnetic simulation[50, 51]. Second, a probability-adjustable TRNG is proposed, in which voltage-controlled magnetic anisotropy (VCMA) effects are controlled by voltage, and an anisotropy gradient is used to obtain desired 0 or 1 ratios. Following the random number calculation, the random 0 and 1 are combined into a truly random number in bitstream through Bernoulli's law of large numbers and a specific logic gate. The application of skyrmion can now be seen from a new perspective. We plan to test the performance of bimeron, another in-plane topological counterpart of magnetic skyrmion, in thermal effects based on our above work. The fact that skyrmion and bimeron have topologically equivalent dynamics and statics, but their statics and dynamics differ, makes them equally attractive from the standpoint of physics and spintronic applications.

3. 1 Mean-squared displacement

We calculate the MSD(mean-squared displacement) from the trajectory to precisely quantify its behavior. MSD calculates the initial position of bimeron, and then calculates the deviation between the position of all subsequent time nodes and the initial position, and finally sums up the average[22]. Two dimensions MSD can be calculated as.

$$MSD = \frac{1}{n}\sum_{i=0}^{n-1}\left[\left(X(t+t^*) - X(t)\right)^2 + \left(Y(t+t^*) - Y(t)\right)^2\right] = 4D_{dc}t^* \quad (3\text{-}1)$$

where t^* being the time between two subsequent events, $n \equiv N_r - t/\Delta t + 1$ is the overlapping segments of time steps to be averaged and N_r is the total number of time steps. $(X(t), Y(t))$ represents the reference position of the skyrmion at the real time t.

3. 2 Example of Brownian motion

This section discusses the thermal Brownian motion of skyrmion and bimeron separately and compares them at the end. In the simulation experiment, we use a circular sample in order to reduce the effects of shape anisotropy on the Brownian dynamics of skyrmion. In addition, in order to better reflect the difference between skyrmion and bimeron, skyrmion and bimeron will conduct simulation experiments under the same conditions at different temperatures. We used the following material parameters: $M_s = 47e\hat{}4\ A/m$, $A = 15pJm^{-1}$, $D = 3.5e\hat{}6\ j/m^2$, $Ku = 0.6e^6 J/m\hat{}3$, alpha=0.05. In this chapter, in order to better reflect the difference between skyrmion and bimeron, skyrmion and bimeron will conduct simulation experiments under the same conditions at different temperatures. At the same time, we record the instantaneous trajectory and velocity of the particle and draw a broken line graph to better reflect the Brownian motion of the particle. Each temperature was simulated under five different random seeds.

$r(t) = (X(t), Y(t))$ is the skyrmion position measured from the space-dependent output file of MUMAX3, the transient velocity is $v(t) = (v_x(t), v_y(t))$

$$v(t) = \frac{\mathrm{d}r(t)}{\mathrm{d}t} = \begin{cases} \mathrm{d}X(t)/\mathrm{d}t = (X(t+\Delta t) - X(t))/\Delta t = v_x(t) \\ \mathrm{d}Y(t)/\mathrm{d}t = (Y(t+\Delta t) - Y(t))/\Delta t = v_y(t) \end{cases} \tag{3-2}$$

The period of time between two consecutive frames is indicated by Δt.

3. 2. 1 Example of skyrmion Brownian motion

Figure 3.1 illustrates, from the simulation result recorded for a skyrmion at several temperatures, the x- and y-components of the skyrmion trajectory $(X(t), Y(t))$, and the transient velocity $(v_x(t), v_y(t))$ with their individual statistical distributions. Here, we study the isolated ferromagnetic skyrmion in $120 \times 120 \times 0.6\ nm$ film, using $120 \times 120 \times 1$ finite difference element discrete. Exchange constant $A = 15pJm^{-1}$, saturation magnetization $M_s = 47e\hat{}4\ A/m$, A vertical magnetic anisotropy constant $Ku = 0.6e\hat{}6 J/m^3$, an interfacial Dzyaloshinskii-Moriya interaction (DMI) constant $D = 0.42e\hat{}6\ j/m^2$, gilbert damped αlpha= 0.05. With (a1), (a2), (a3), (a4) and (a5) are trajectory $(X(t), Y(t))$ of skyrmion of 20K, 40K, 60K, 80K and 100K respectively, (b) and (c) represent cumulative distribution functions (CDF) and probability density functions (PDF), respectively. CDF describes the distribution of probabilities for random variables of trajectory and PDF describes the probability that the value of a random trajectory falls within the region. For all real numbers x, the cumulative distribution function is defined as follows:

$$F_X(x) = \mathrm{P}(X \leq x). \tag{3-3}$$

Here suppose X is uniformly distributed on the unit interval $[0,1]$. For the one-dimensional real random variable X, let its cumulative distribution function be X.[52] If there is a measurable function $f_X(x)$, it satisfies:

$$\forall -\infty < a < \infty, F_X(a) = \int_{-\infty}^{a} f_X(x)dx. \tag{3-4}$$

Then X is a continuous random variable, and $f_X(x)$ is its probability density functions. In this section, X indicates trajectory.

(a1) 20K

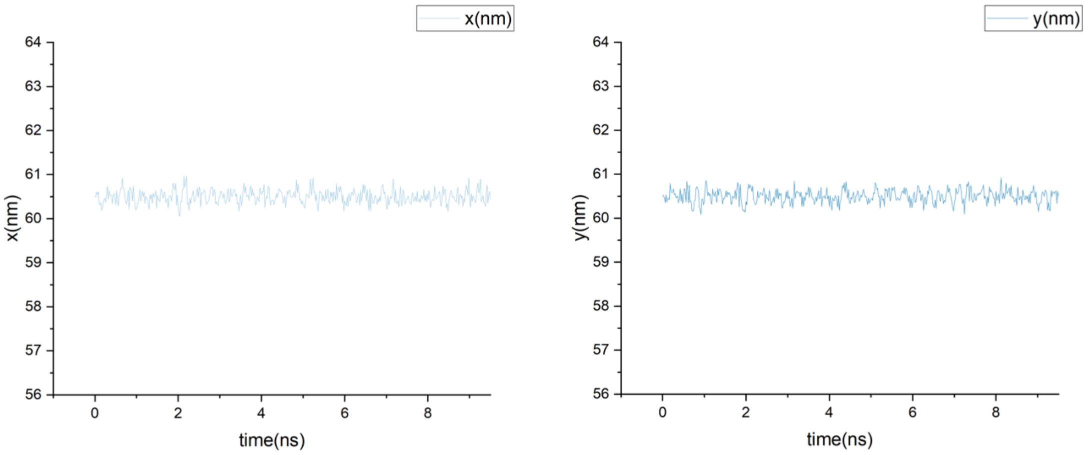

(a2) 40K

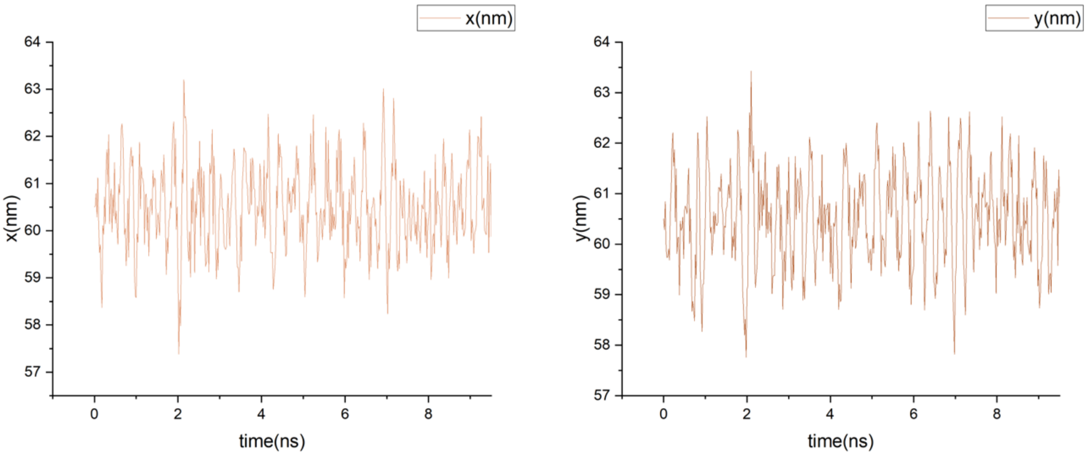

(a3) 60K

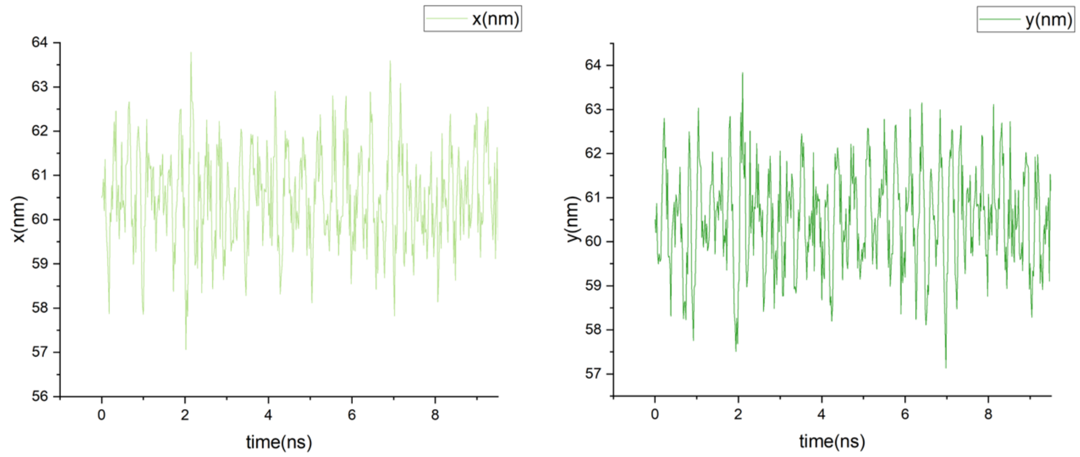

(a4) 80K

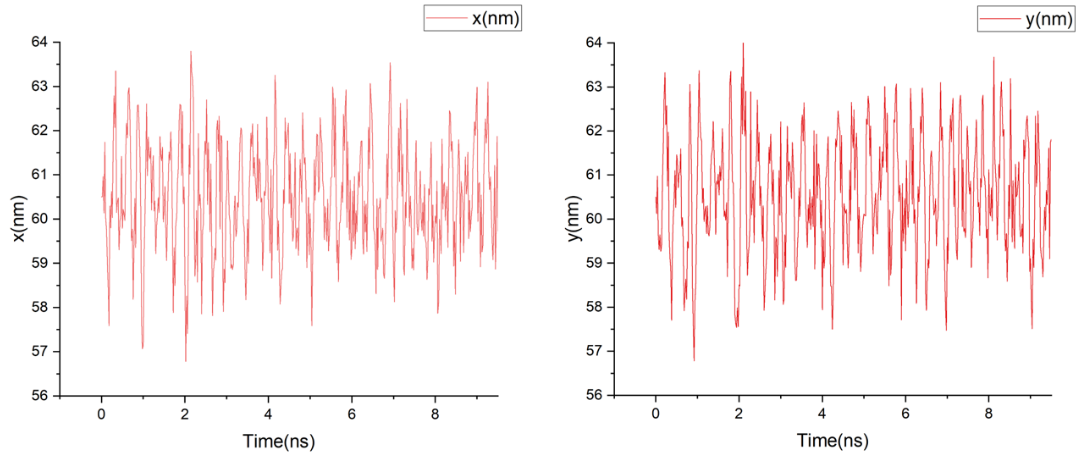

(a5) 100K

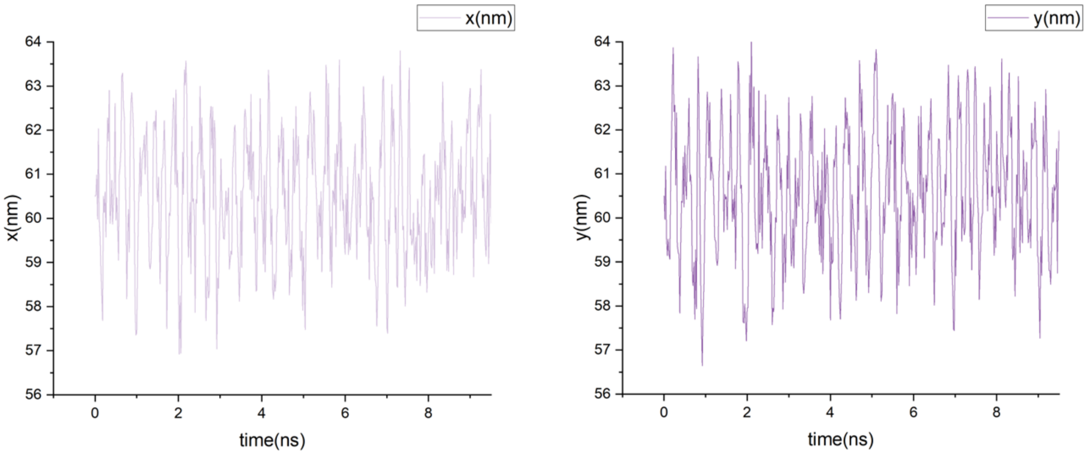

(b) CDF

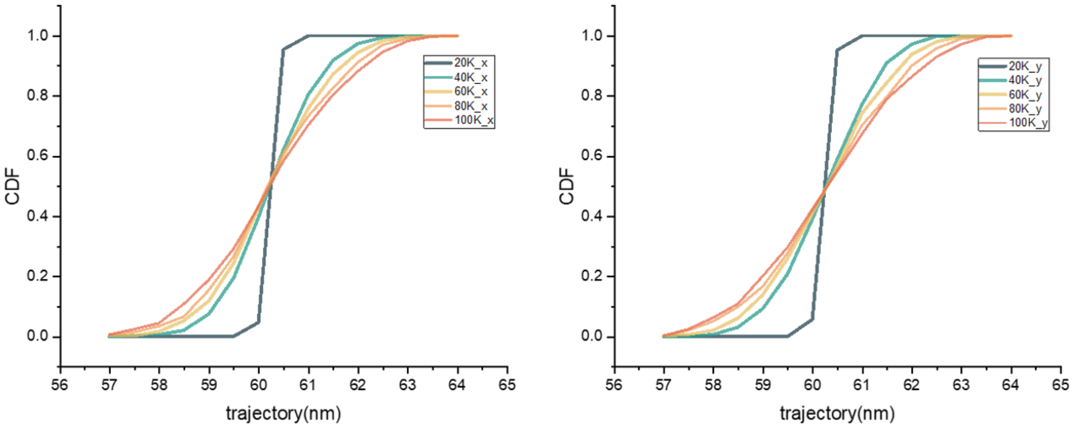

(c) PDF

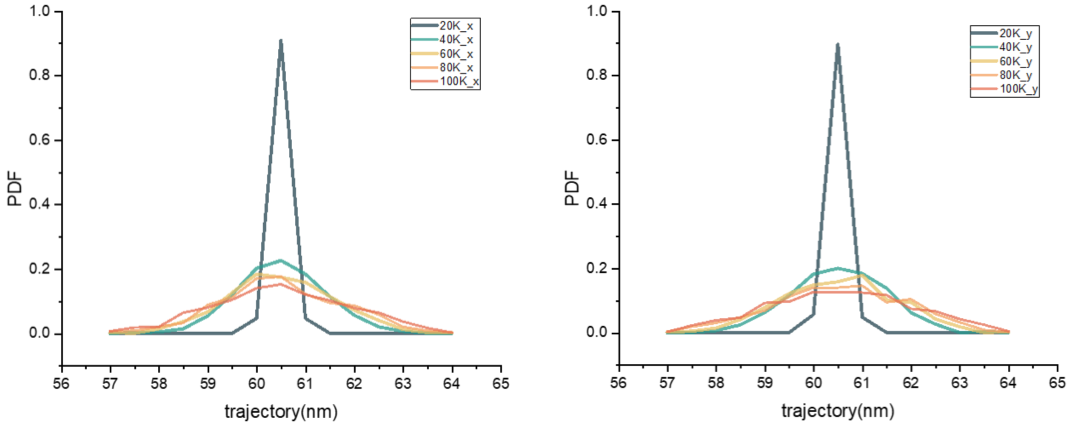

Figure 3.1 (a1) to (a5): Trajectories of the x- and y-components of the diffusive skyrmions and their cumulative frequency and relative frequency in (b) and (c).

Figure 3.1(a1)-(a5) illustrate the trajectory of Brownian motion in the X and Y directions of skyrmion at different temperatures of 20K, 40K, 60K, 80K, and 100K. The trajectory is very gentle at 20K, as can be seen in figure 3.1(a1). As the temperature increases from 40K to 100K, the trajectory changes dramatically. The trajectory of the skyrmion changes roughly in accordance with the temperature. Overall, the X-axis and the Y-axis change about the same amount. As shown in figure 3.1(b) and (c), the probability density of a trajectory is calculated. The trajectory mainly ranges from 60mm to 61mm when the temperature is 20K. As the temperature rises, the trajectory changes gradually and the distribution ranges from 57mm to 64mm. This indicates again the randomness of the Brownian motion of the soliton. The Gaussian distribution is well suited to fit the PDF of the instantaneous position of the soliton.

Figure 3.2 shows, based on simulation results recorded for a skyrmion at several temperatures, the x- and y-components of the skyrmion transient velocity with their respective statistical distributions. There are five velocities of skyrmions for 20K, 40K, 60K, 80K, and 100K, respectively. (e) and (f) are theoretical cumulative distribution functions (CDF) and probability density functions (PDF). As illustrated in figure 3.1, CDF, and PDF describe the probability distribution of random variables.

(a1) 20K

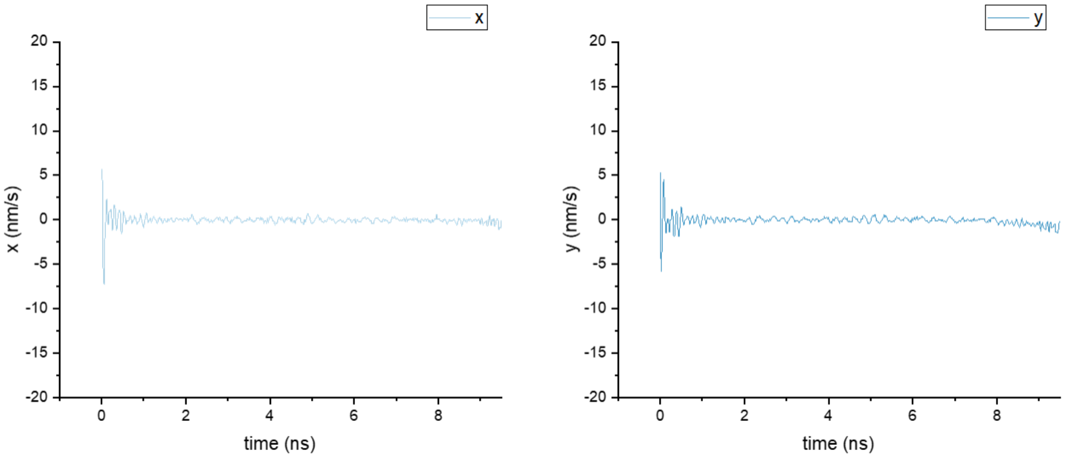

(a2) 40K

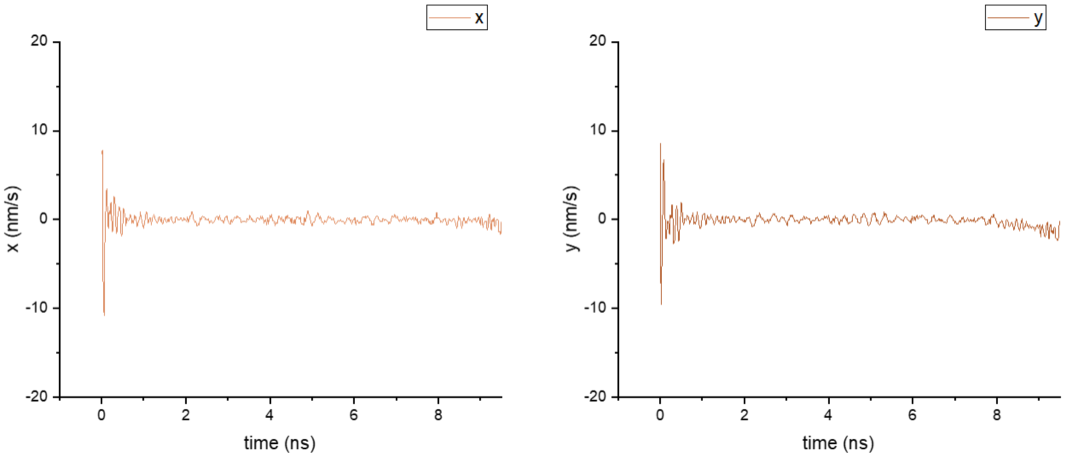

(a3) 60K

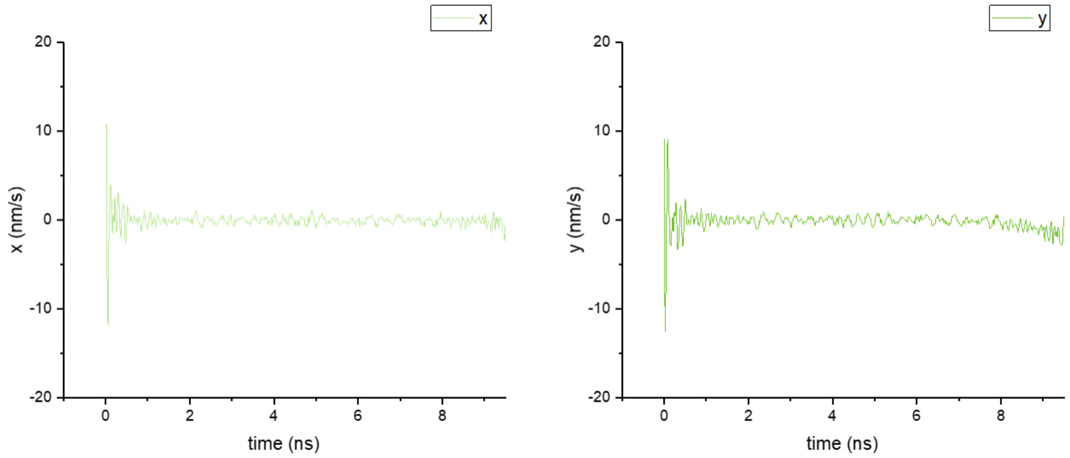

(a4) 80K

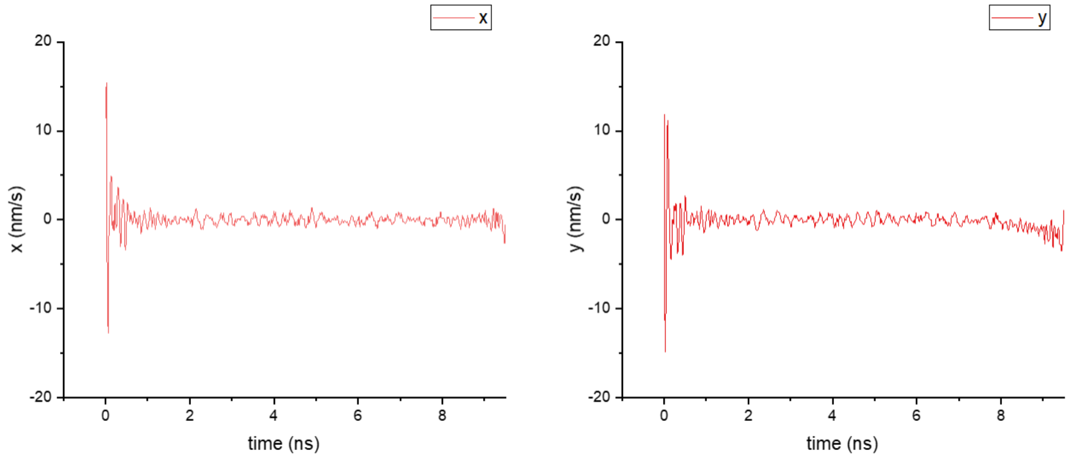

(a5) 100K

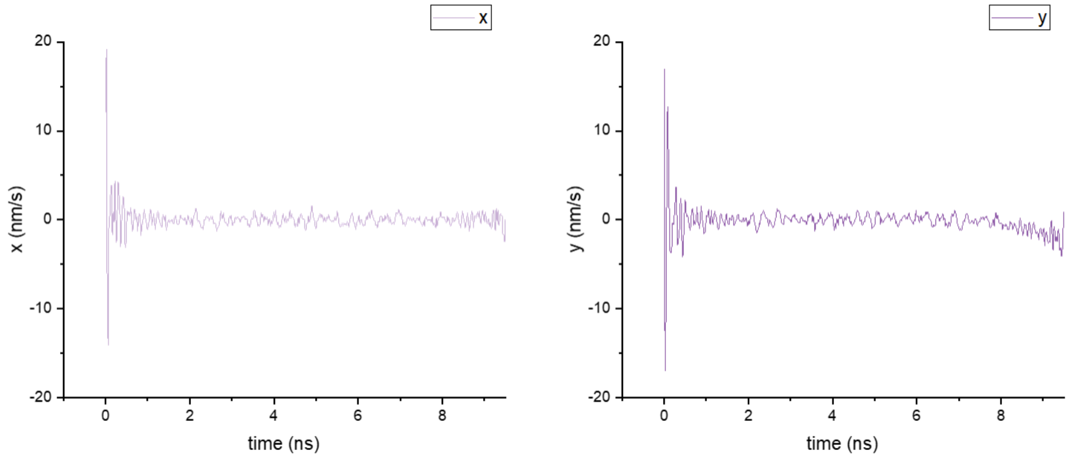

(b) CDF

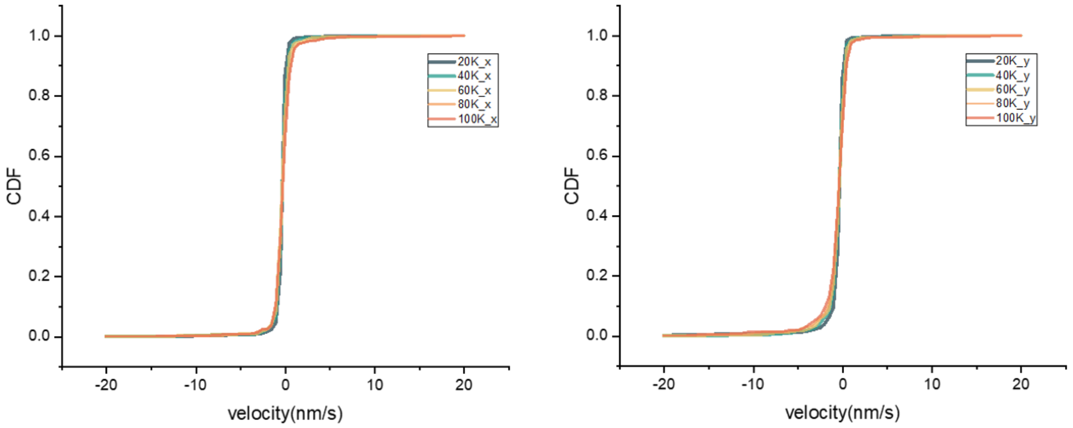

(c) PDF

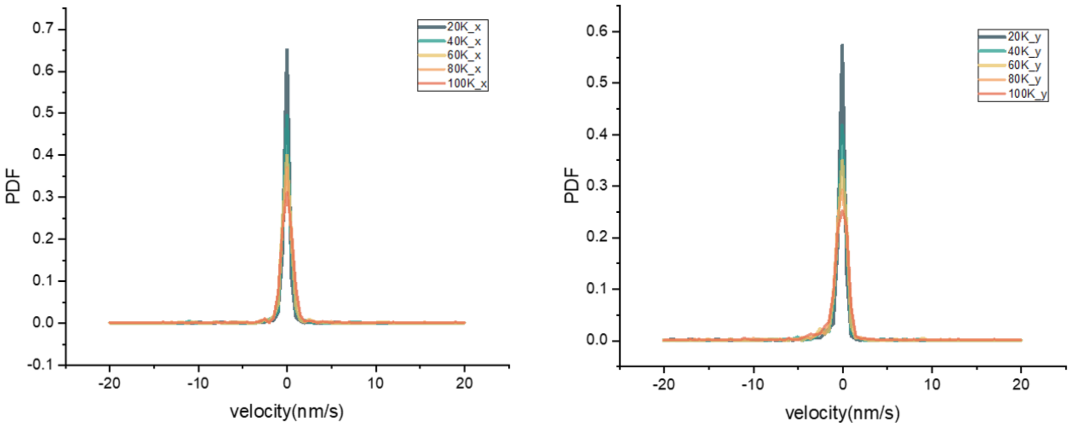

Figures 3.2 (a1)-(a5) Illustrate the velocities of the x- and y-components as v(x) and v(y) and their distribution frequencies in (b) and (c), respectively.

Figure 3.2(a1)-(a5) represents skyrmion's instantaneous velocity. The y axis of the particle was affected by the thermal effect at the beginning of the simulation, so the violent jitter could be ignored. The figure illustrates that the instantaneous velocity of Brownian motion of skyrmion is not violent and that the variation range of instantaneous velocity only gradually increases with temperature. In the meantime, the X-axis and Y-axis velocity components of skyrmion are approximately the same. As the PDF and CDF changes in fig.2.3 (b) and (c) are combined, it can be seen that the velocity changes tend toward zero at low temperature while the velocities on the X-axis and Y-axis increase slightly as the temperature rises. Thus, the soliton velocity is relatively insensitive to thermal effects. As shown in figure 3.2(c), at 20K, the velocity is generally 0mm/s, while at 100K, the velocity is significantly less, averaging -0.5mm/s-+0.5mm/s. Similarly, the Gaussian distribution can well fit the PDF of the instantaneous velocity of the soliton, confirming the randomness of the Brownian motion of the skyrmion.

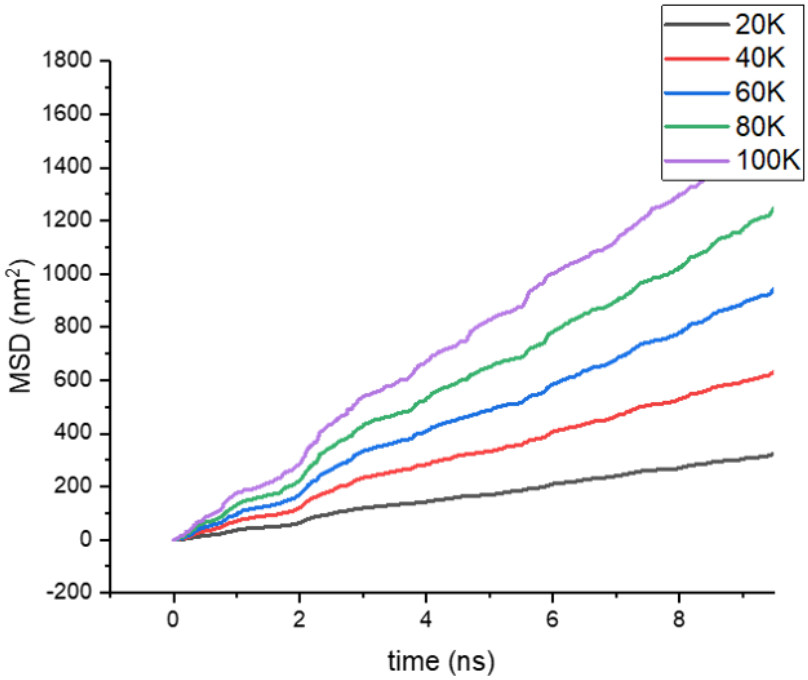

Figure 3.3 Results of the temperature-dependent MSD curves, illustrate the MSD increase linearly and continuously where time becomes larger.

Figure 3.3 depicts the MSD changes of skyrmion at different temperatures. As temperature increases, the MSD of particles also increases, meaning that the diffusion range of particles on the sample also increases as temperature increases. We use a circular sample in the simulation experiment in order to reduce the effects of shape anisotropy on the Brownian dynamics of the skyrmion. Due to the defect, skyrmion was unable to spread its thermal motion throughout the sample. Specifically, skyrmion was not able to reach all parts of the sample during the actual duration of the experiment at lower temperatures. As can be seen in figure 3.3, the area of skyrmion reached by skyrmion increases with increasing temperature.

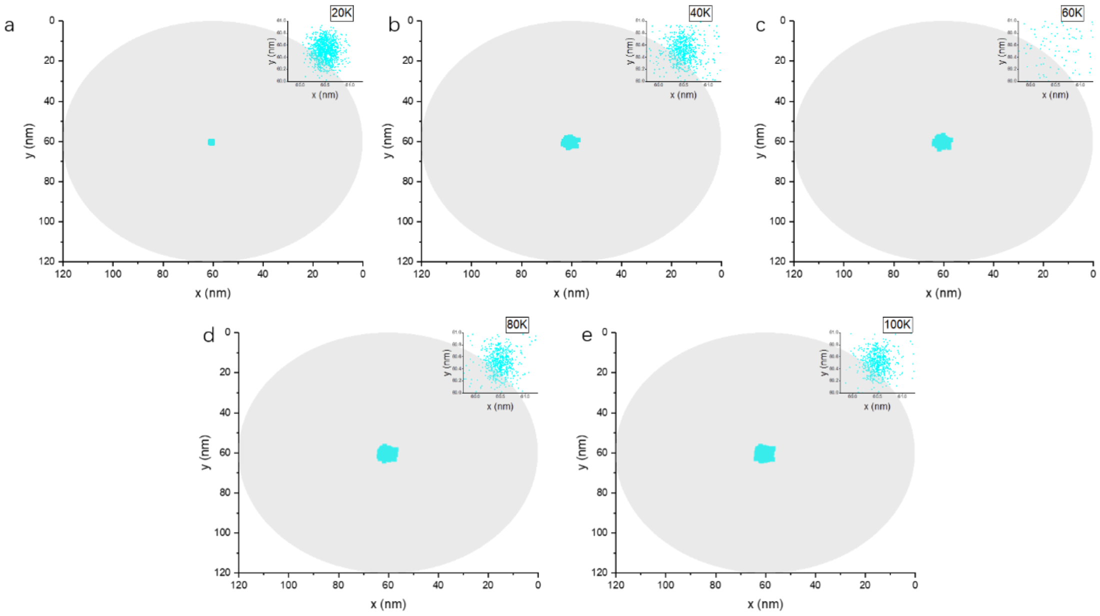

Figure 3.4 Probability of skyrmion occurrence at various temperatures. At higher temperatures, skyrmion is able to attain a larger area on the sample, as shown by the more widespread distribution of data points.

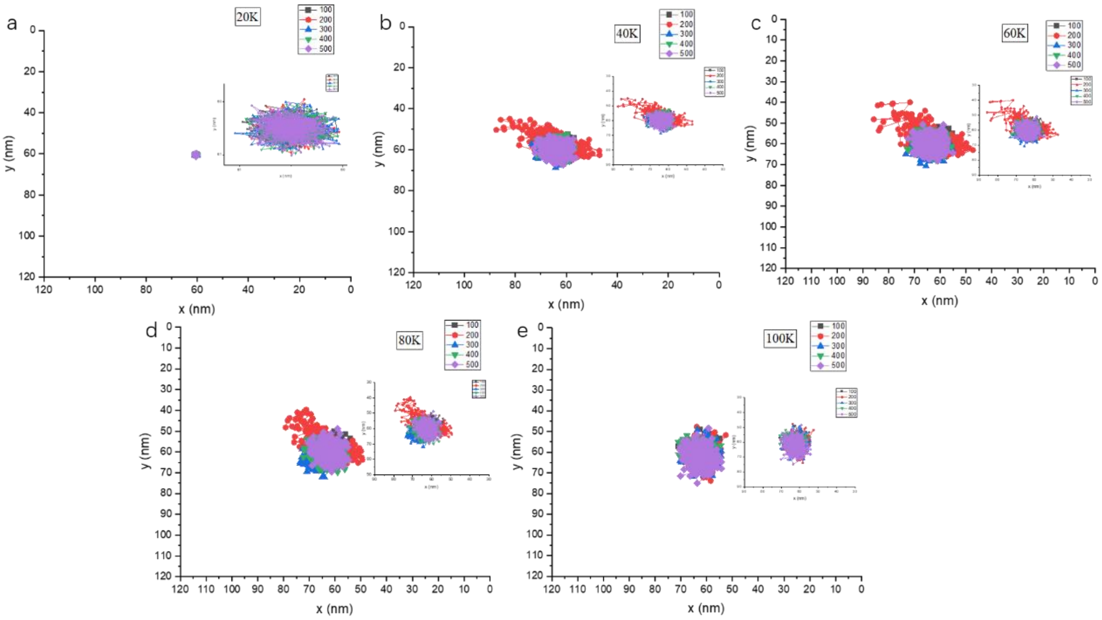

Figure 3.5 Simulated Brownian-motion trajectories of a single isolated skyrmion for different random seeds at (a) T = 20 K, (b) T = 40 K, (c) T = 60 K, (d) T = 100K and (d) T = 80 K.

As illustrated in figure 3.5, we independently simulate Brownian motion for a single soliton at different temperatures using different random numbers. With a given temperature, the soliton shows a different trajectory for different random numbers, and the amplitude of soliton diffusion is independent of the random number.

3. 2. 2 Example of bimeron Brownian motion

In this chapter, we describe the bimeron by separating the two merons of the bimeron with q = +1 and q = -1, corresponding to spin-up merons and spin-down merons, respectively. Here we analyze the isolated ferromagnetic bimeron, discrete with a $120 \times 120 \times 1\,nm$ finite-difference element, in a $120 \times 120 \times 0.6\,nm$ film. Exchange constant $A = 15pJm^{-1}$, saturation magnetization $M_s = 47e\hat{}4\,A/m$, A vertical magnetic anisotropy constant $Ku = 0.6e\hat{}6\,J/m^3$, an interfacial Dzyaloshinskii-Moriya interaction (DMI) constant $D = 0.42e\hat{}6j/m^2$, gilbert damped αlpha= 0.05. To provide a better comparison with skyrmion, bimeron's simulated sample and parameter environment are in line with skyrmion's above. The figure 3.6(a1)-(a5) illustrates the changes in the trajectory of the bimeron at 20K, 40K, 60K, 80K, and 100K, respectively. As a result, the x and y axes of the meron with spin up and spin down are calculated, as well as the overall x and y trajectories of the bimeron. Figure 3.6(b) and (c) illustrate the calculation of the statistical distribution of each component and bimeron particle.

(a1) 20K

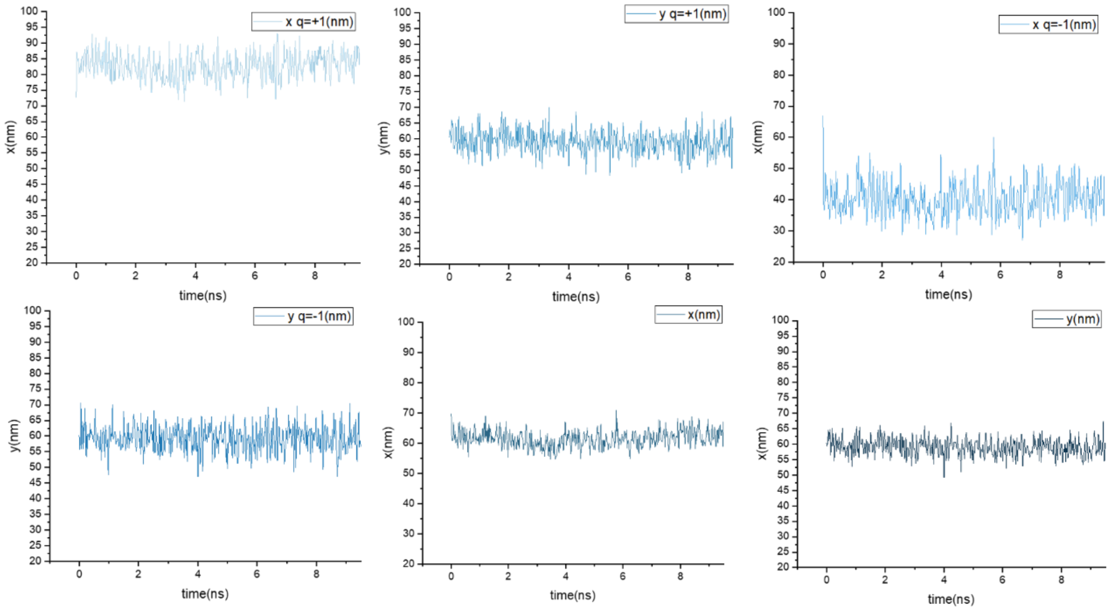
x q=+1(nm)
x(nm)
time(ns)
y q=+1(nm)
y(nm)
time(ns)
x q=-1(nm)
x(nm)
time(ns)
y q=-1(nm)
y(nm)
time(ns)
x(nm)
x(nm)
time(ns)
y(nm)
x(nm)
time(ns)

(a2) 40K

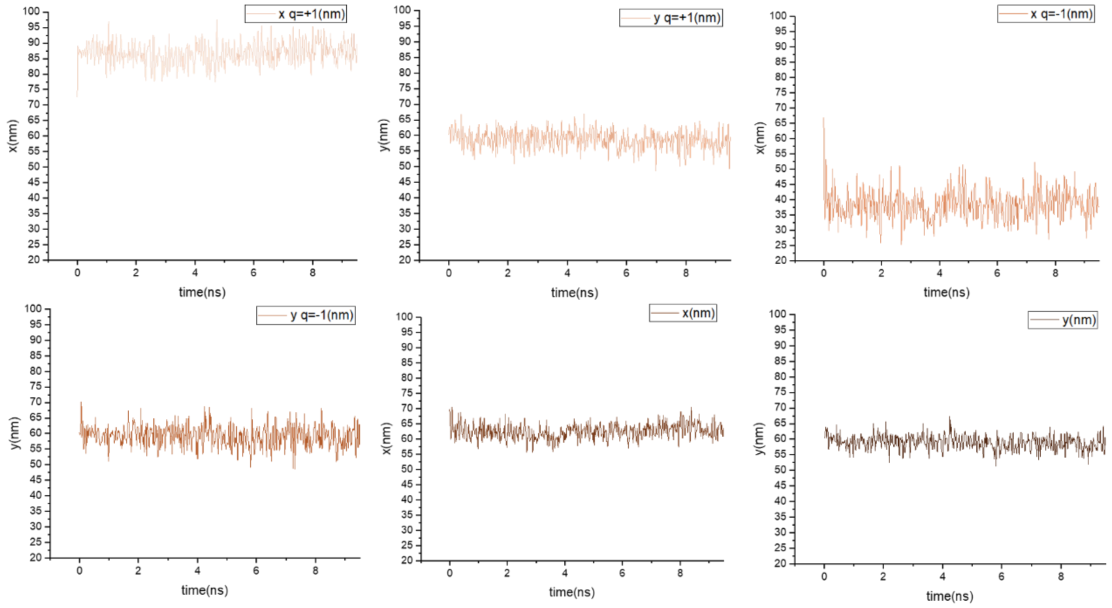
x q=+1(nm)
x(nm)
time(ns)
y q=+1(nm)
y(nm)
time(ns)
x q=-1(nm)
x(nm)
time(ns)
y q=-1(nm)
y(nm)
time(ns)
x(nm)
x(nm)
time(ns)
y(nm)
y(nm)
time(ns)

(a3) 60K

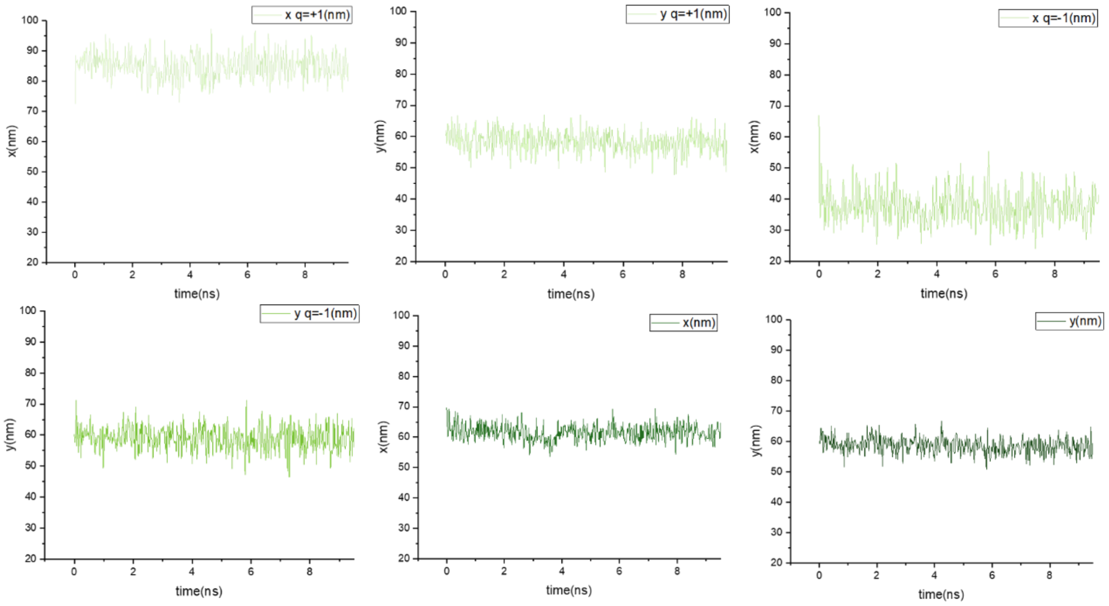
x q=+1(nm)
x(nm)
time(ns)
y q=+1(nm)
y(nm)
time(ns)
x q=-1(nm)
x(nm)
time(ns)
y q=-1(nm)
y(nm)
time(ns)
x(nm)
x(nm)
time(ns)
y(nm)
y(nm)
time(ns)
20
30
40
50
60
70
80
90
100
0
2
4
6
8

(a4) 80K

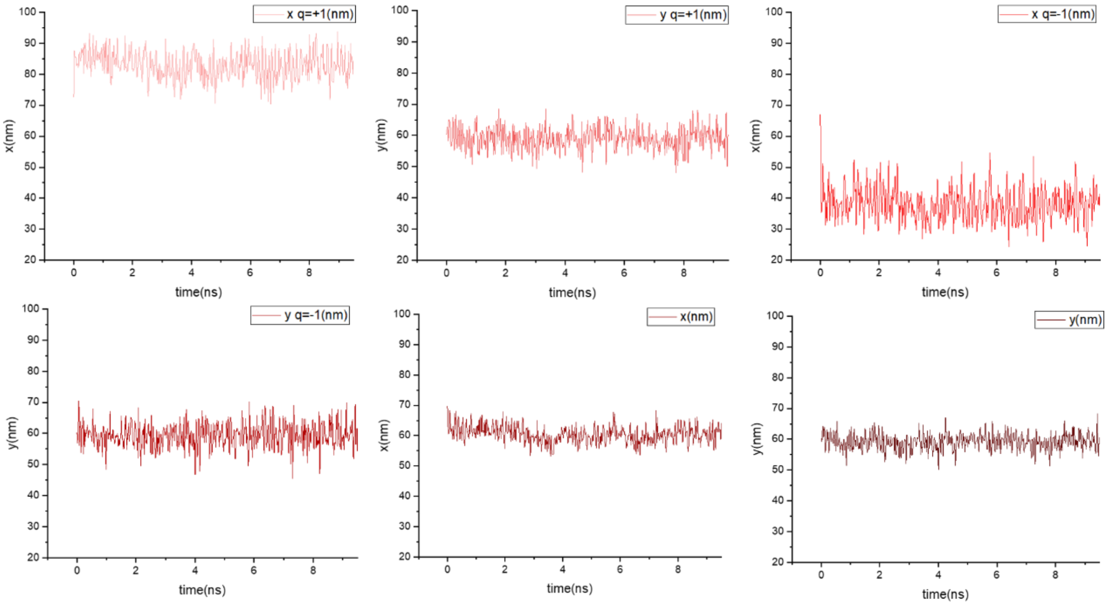
x q=+1(nm)
x(nm)
time(ns)
y q=+1(nm)
y(nm)
time(ns)
x q=-1(nm)
x(nm)
time(ns)
y q=-1(nm)
y(nm)
time(ns)
x(nm)
x(nm)
time(ns)
y(nm)
y(nm)
time(ns)
20
30
40
50
60
70
80
90
100
0
2
4
6
8

(a5) 100K

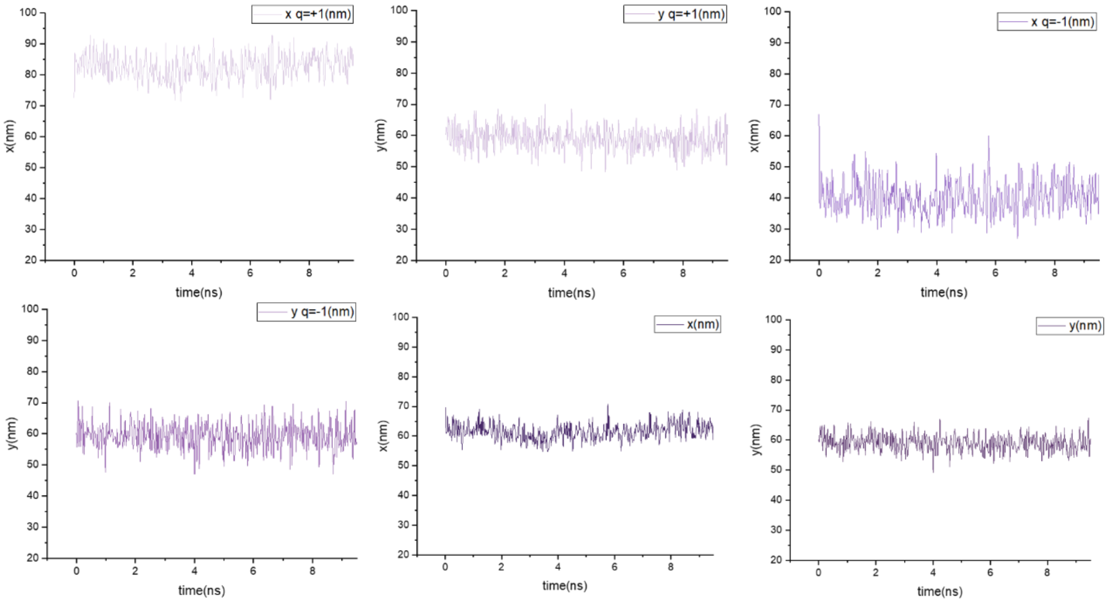
x q=+1(nm)
y q=+1(nm)
x q=-1(nm)
y q=-1(nm)
x(nm)
y(nm)
x(nm)
y(nm)
time(ns)
0
2
4
6
8
20
30
40
50
60
70
80
90
100

(b) CDF

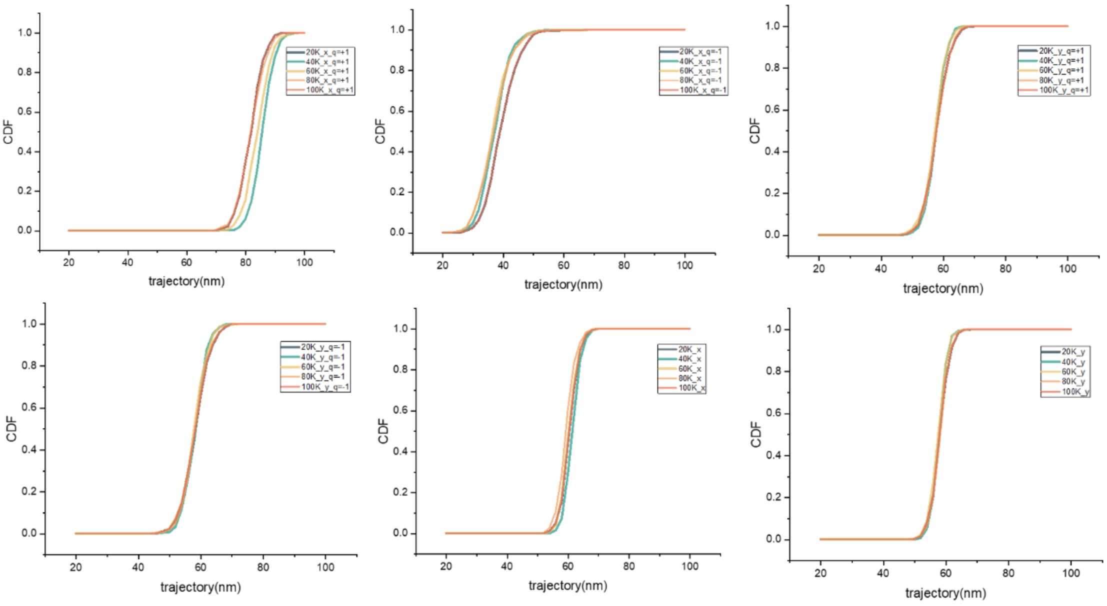
20K_x_q=+1
40K_x_q=+1
60K_x_q=+1
80K_x_q=+1
100K_x_q=+1
20K_x_q=-1
40K_x_q=-1
60K_x_q=-1
80K_x_q=-1
100K_x_q=-1
20K_y_q=+1
40K_y_q=+1
60K_y_q=+1
80K_y_q=+1
100K_y_q=+1
20K_y_q=-1
40K_y_q=-1
60K_y_q=-1
80K_y_q=-1
100K_y_q=-1
20K_x
40K_x
60K_x
80K_x
100K_x
20K_y
40K_y
60K_y
80K_y
100K_y
CDF
trajectory(nm)
0.0
0.2
0.4
0.6
0.8
1.0
20
40
60
80
100

(c) PDF

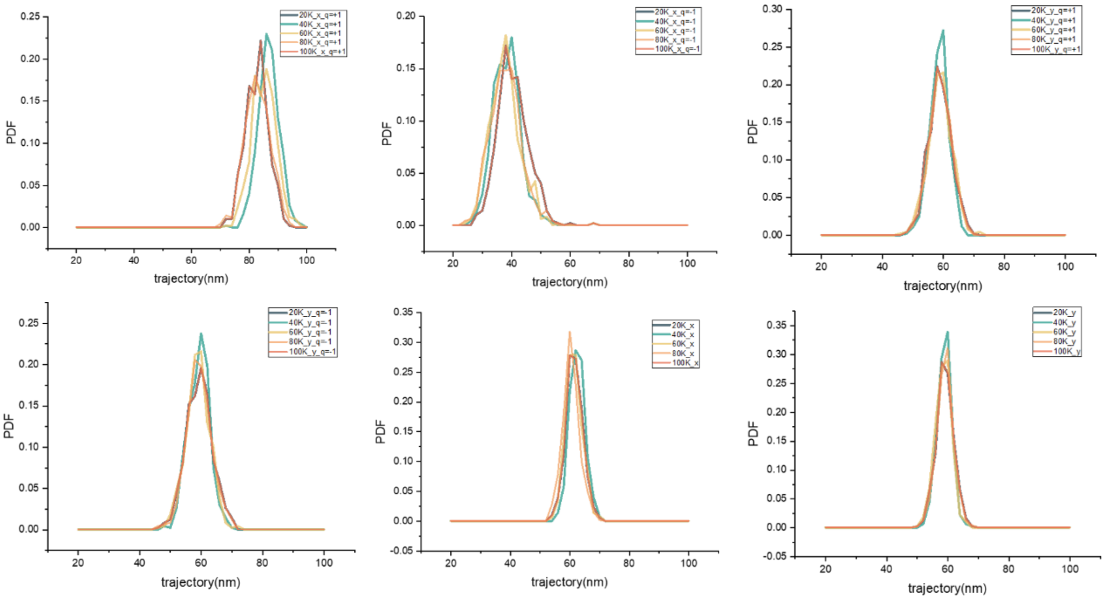

Figure 3.6 (a1)-(a5) Depict the X- and Y-axis trajectories of a meron with Q=+1 and a meron with Q=-1 in bimeron. (b)(c) Diagram illustrating the trajectory for cumulative frequency and relative frequency of bimeron and each meron at the X- and Y-axes.

Figure 3.6 (a1)-(a5) illustrates that when the X-axis component of meron with upward spin is subjected to the thermal effect, the trajectory value is larger for meron with downward spin than for meron with upward spin. Moreover, the Y-axis component of Q=+1 and Q=-1 has roughly the same value. Figure 3.6(c) PDF behavior is not uniform, the bimeron's instantaneous displacement does not follow a Gaussian distribution. According to figure 3.6(c), the trajectory distribution of the x axis of meron with Q=+1 mainly ranges from 80nm to 85nm, and for meron with Q=-1 mainly ranges from 40nm. The Y-axis trajectory of each meron is approximately 60nm. Temperature differences are primarily evident in the X-axis trajectory of each meron. The trajectory of the X axis of each meron is relatively close to one another as the temperature rises.

(a1) 20K

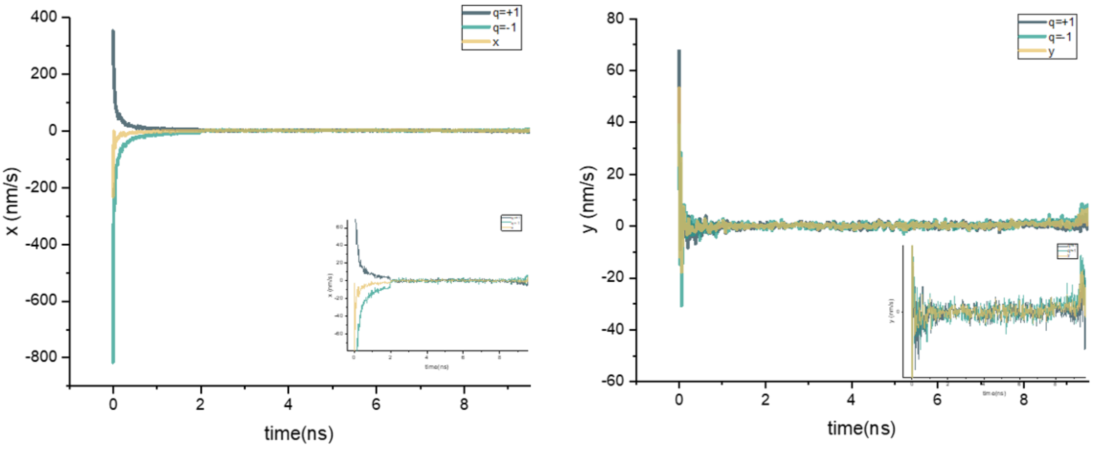

(a2) 40K

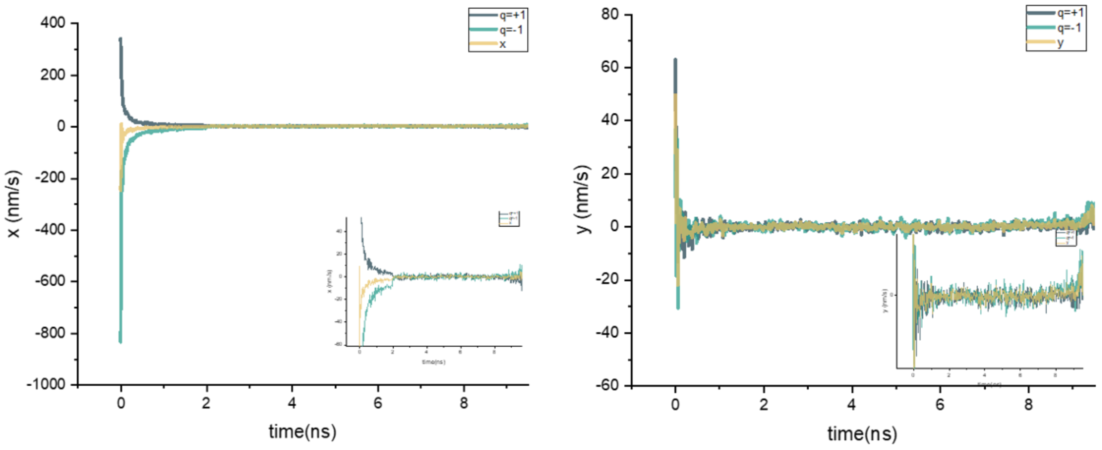

(a3) 60K

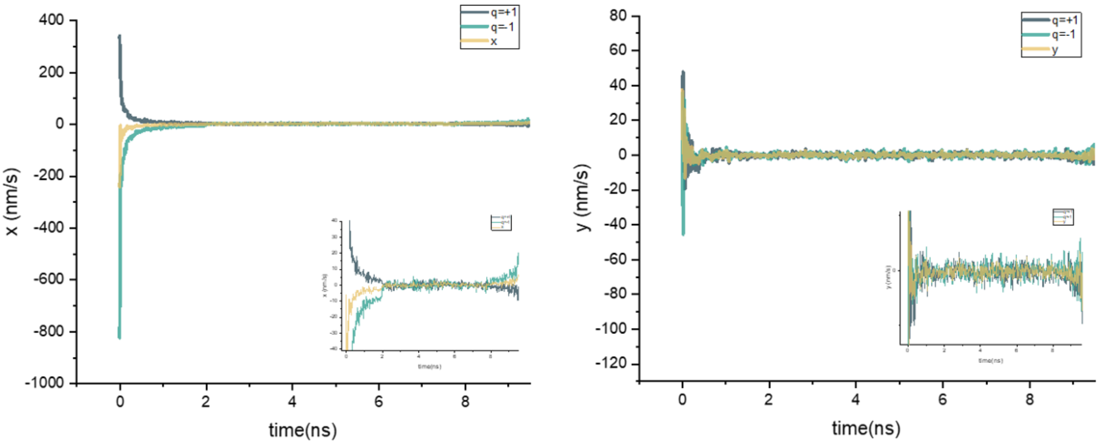

(a4) 80K

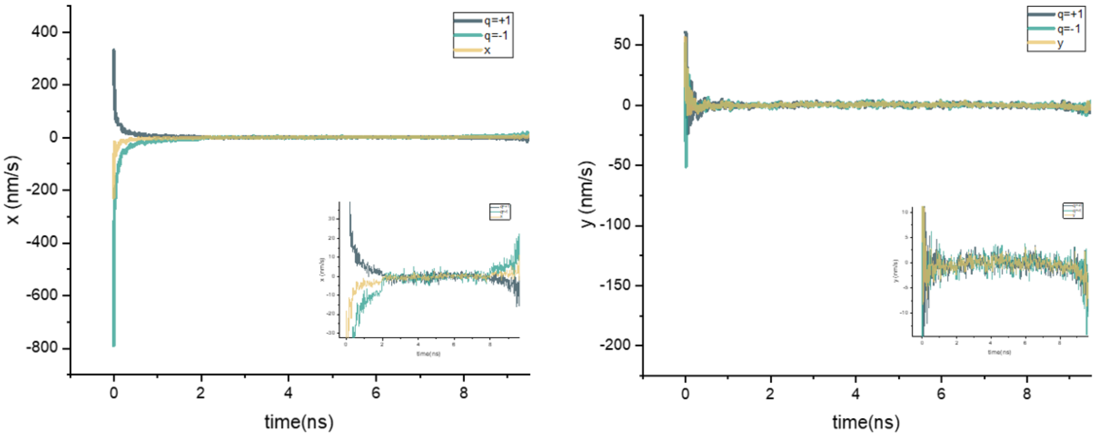

(a5) 100K

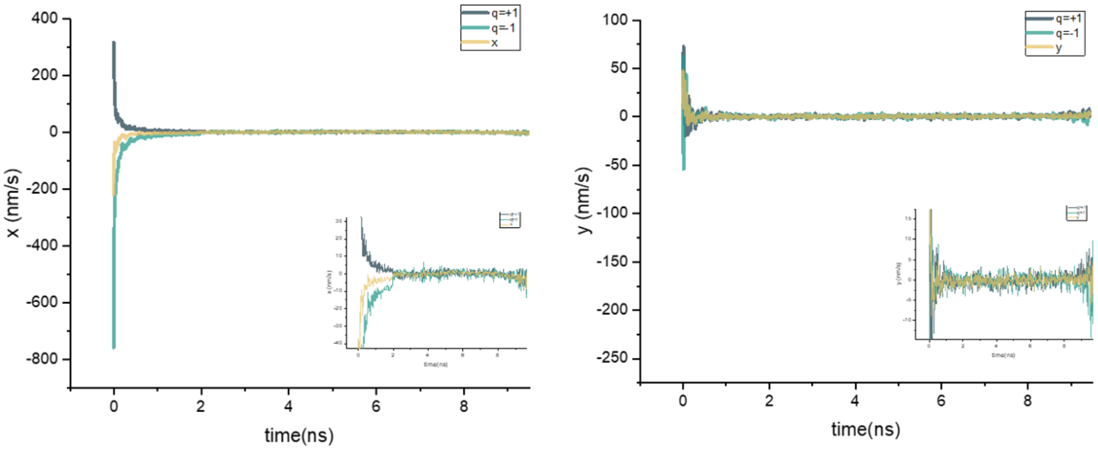

(b) CDF

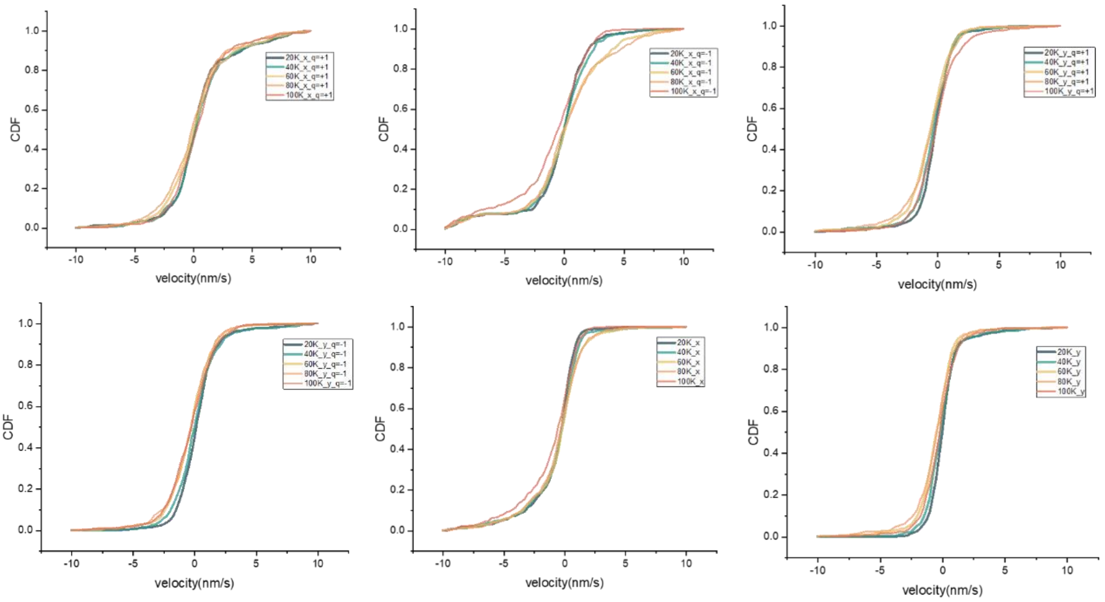
CDF
velocity(nm/s)
20K_x_q=+1
40K_x_q=+1
60K_x_q=+1
80K_x_q=+1
100K_x_q=+1
20K_x_q=-1
40K_x_q=-1
60K_x_q=-1
80K_x_q=-1
100K_x_q=-1
20K_y_q=+1
40K_y_q=+1
60K_y_q=+1
80K_y_q=+1
100K_y_q=+1
20K_y_q=-1
40K_y_q=-1
60K_y_q=-1
80K_y_q=-1
100K_y_q=-1
20K_x
40K_x
60K_x
80K_x
100K_x
20K_y
40K_y
60K_y
80K_y
100K_y
0.0
0.2
0.4
0.6
0.8
1.0
-10
-5
0
5
10

(c) PDF

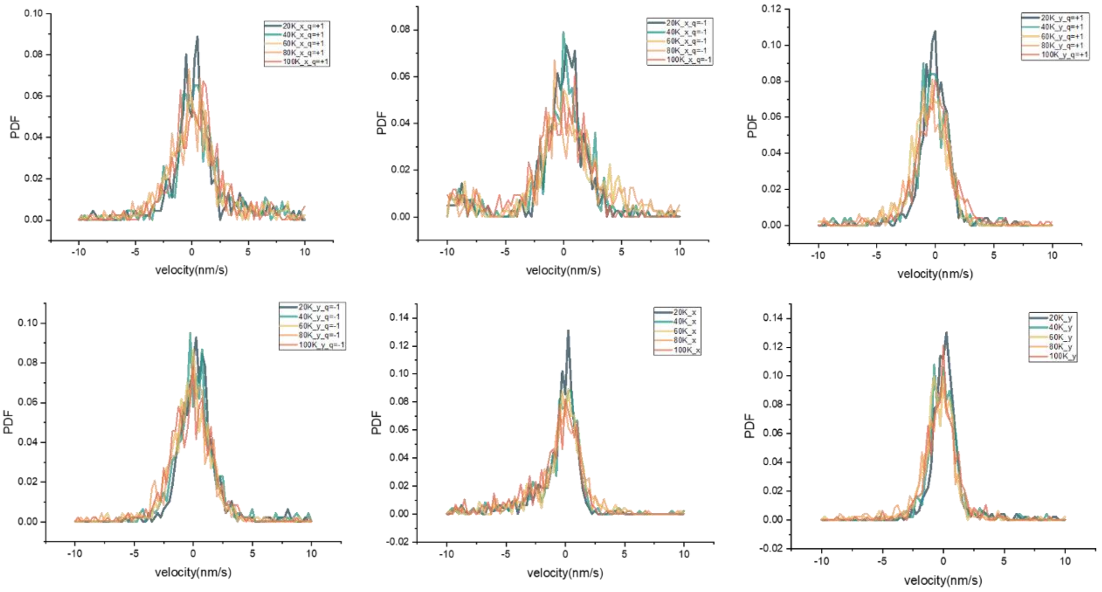
PDF
velocity(nm/s)
20K_x_q=+1
40K_x_q=+1
60K_x_q=+1
80K_x_q=+1
100K_x_q=+1
20K_x_q=-1
40K_x_q=-1
60K_x_q=-1
80K_x_q=-1
100K_x_q=-1
20K_y_q=+1
40K_y_q=+1
60K_y_q=+1
80K_y_q=+1
100K_y_q=+1
20K_y_q=-1
40K_y_q=-1
60K_y_q=-1
80K_y_q=-1
100K_y_q=-1
20K_x
40K_x
60K_x
80K_x
100K_x
20K_y
40K_y
60K_y
80K_y
100K_y
-0.02
0.00
0.02
0.04
0.06
0.08
0.10
0.12
0.14
-10
-5
0
5
10

(d) statistical test

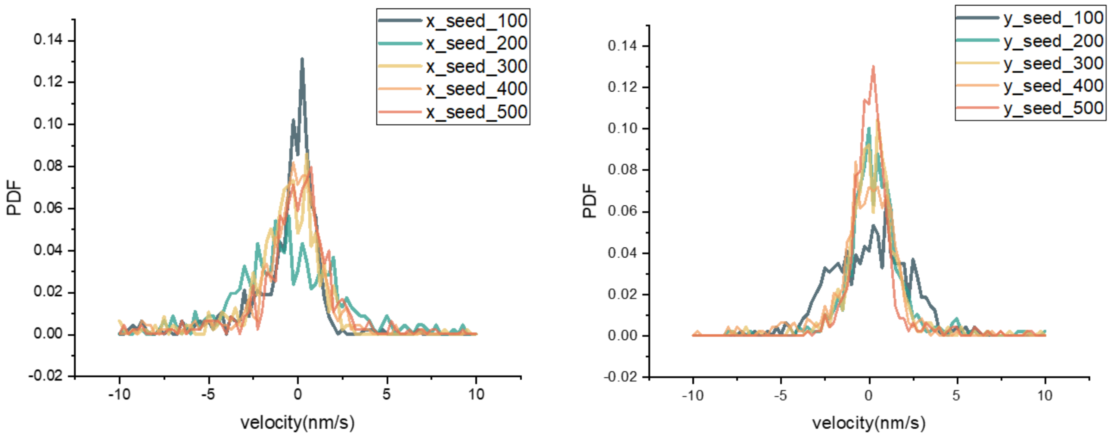

Figure 3.7 (a1)-(a5) Illustrate the velocities of the x- and y-components as v(x) and v(y) and their distribution frequencies in (b) and (c), respectively. (d) Provide a description of the distribution frequencies of the x- and y-axis velocities for five different random seeds at 60 K.

According to figure 3.7, the instantaneous velocity will change dramatically at the beginning of the simulation due to thermal effects, and the meron with q=+1 will produce an opposite velocity to that of the meron with q=-1. Figures 3.7(b) and (c) illustrate that the bimeron's instantaneous velocity does not match the uniform variability of the Gaussian distribution curve, and therefore the bimeron's instantaneous velocity does not match the Gaussian distribution. Under the influence of the thermal effect, the bimeron's instantaneous velocity will be random. In the X-axis direction, the instantaneous velocity of Q=+1 and Q=-1 meron is significantly different as the temperature rises. According to figure (c), at 60K-100K, the peak value of Q=+1 meron is close to -1 and 1, and the peak value of Q=-1 meron is still close to 0. This indicates that the instantaneous velocity of Q=+1 is highly likely to be greater than the instantaneous velocity of Q=-1. According to figures 3.7(d), the Gaussian noise of MUMAX3 corresponds to a Gaussian distribution, whereas under different random seed frequencies, the velocity distribution frequency varies greatly. Due to the weak topology protection of the bimeron, its deformation speed will be disorderly and violent as a result of the thermal effect.

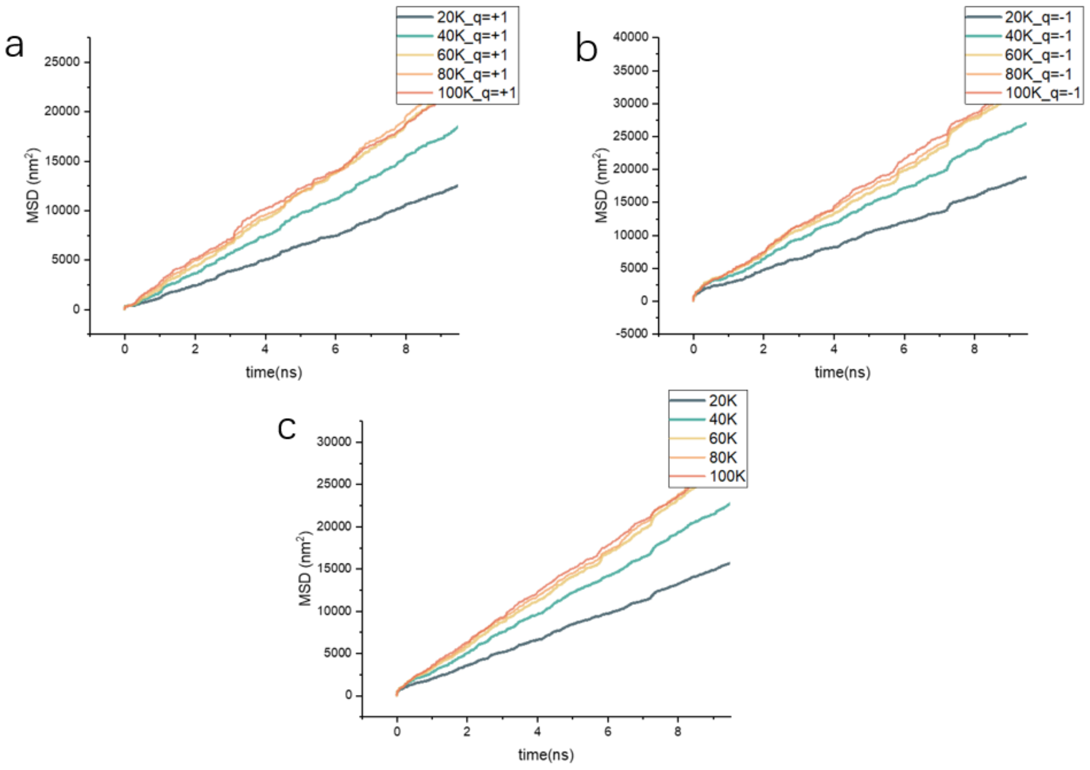

Figure 3.8 (a) to (c): The MSD curve of 20K-60K illustrates that MSD increases linearly and continuously over time. With a temperature rise from 60K to 100K, MSD reaches its limit and does not continue to increase.

Figure 3.8 illustrates the MSD of the bimeron and the MSD of each meron. In the range of 20K to 60K, the MSD of the bimeron and meron gradually increases. The MSD changes at the same rate and value when the temperature exceeds 60K.

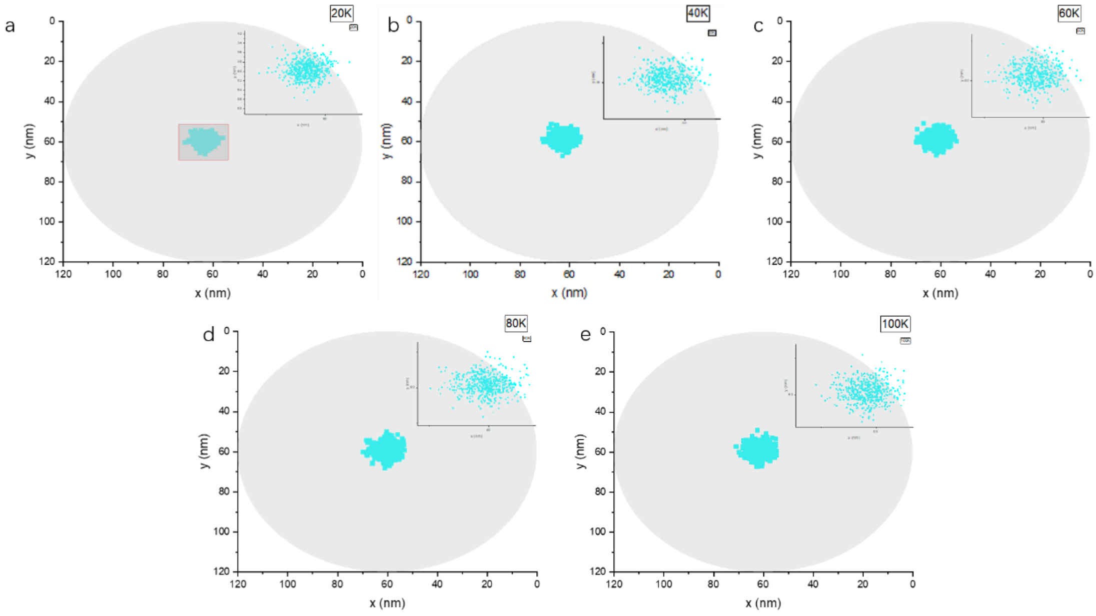

Figure 3.9 (a) to (e): Probability of bimeron occurrence at various temperatures. At higher temperatures, bimeron is able to attain a larger area on the sample, as shown by the more widespread distribution of data points.

According to figure 3.9, bimeron's experimental sample has the same size as skyrmion's experimental sample. As the temperature is raised, the bimeron trajectory tends to expand. With respect to figure 3.8, figure 3.9(a), (b) and (c) demonstrate that the bimeron's diffusion range changes with temperature while (c), (d), and (e) successfully demonstrate that the diffusion range does not change significantly after 60 K is reached.

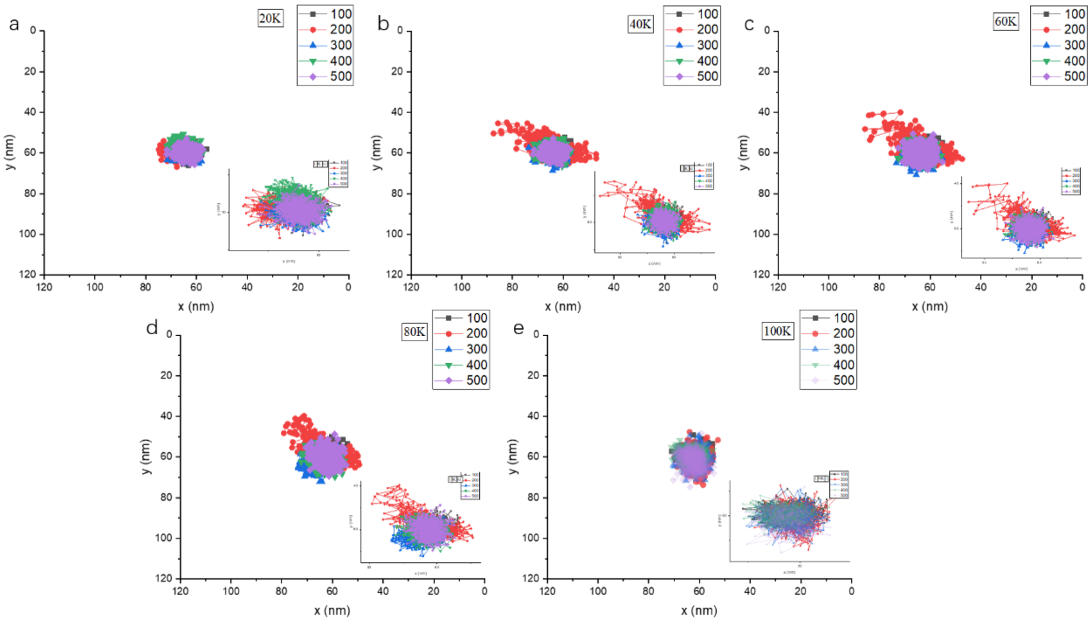

Figure 3.10 (a1) to (a5): Simulated Brownian-motion trajectories of a single isolated bimeron for different random seeds at (a) T = 20 K, (b) T = 40 K, (c) T = 60 K, (d) T = 100K and (d) T = 80 K.

Figure 3.10 illustrates an independent simulation of Brownian motion of a single bimeron based on different random numbers at different temperatures. The bimeron exhibits different trajectory behavior at a given temperature for different random numbers, and the amplitude of bimeron diffusion is independent of random numbers.

3. 2. 3 Brownian motion comparison between skyrmion and bimeron

Using skyrmion and bimeron in the same particle size and parameters environment, we calculate the MSD and instantaneous velocity through the instantaneous displacement of particles (Formula 3-1), in order to compare the difference between their thermal Brownian motions. Furthermore, the topological number of particles was quantified using a lattice-based approach. At a temperature of 120 K, Brownian motion of two particles was simulated by ten random seeds, and the effect of each particle on the thermal effect was observed. Finally, the average topological number is calculated to compare the thermal stability of skyrmion and bimeron.

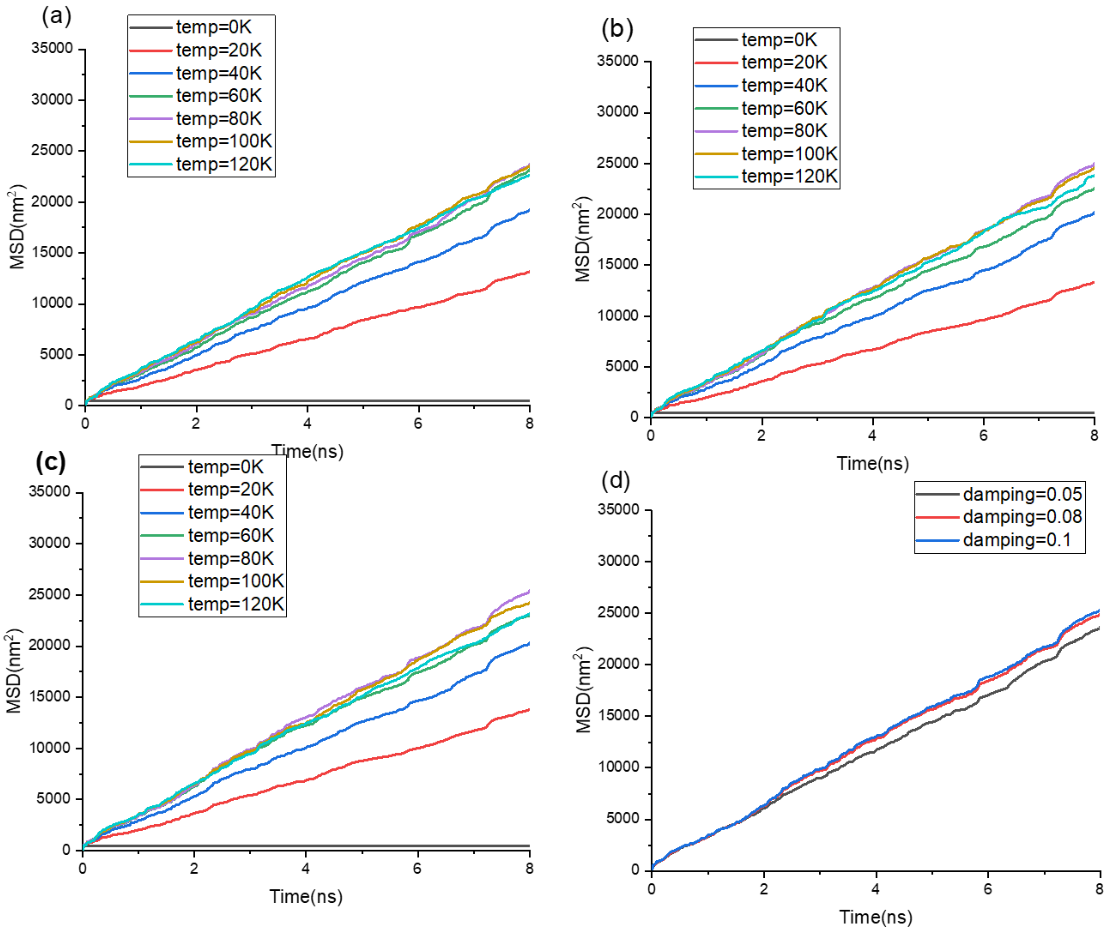

Figure 3.11 Simulated Brownian-motion MSD of a single bimeron for different damping at (a) a = 0.05 (b) a = 0.08 (c) a = 0.1. Simulated performance of three damping. Here, T = 80K.

As shown in figure 3.11, The size of the simulated sample is a circular nanodot of diameter 2 R_d = 120nm and thickness of 1 nm. We performed systematic micromagnetic simulations to calculate each meron of the bimeron MSD of temperature (from 0 to 120K). We used the following material parameters: $M_s = 47e\text{^}4\ A/m$, $A = 15pJm^{-1}$, $D = 3.5e\text{^}6\ j/m^2$, $Ku = 0.4e\text{^}6\ J/m^3$. A single bimeron will do random exercise at various temperatures.

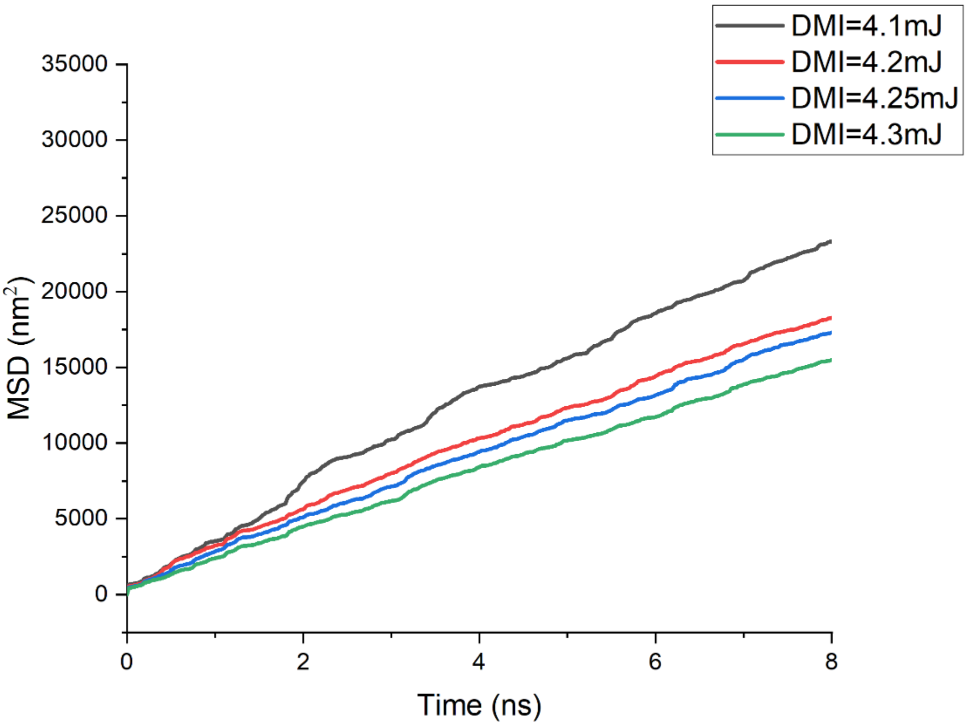

Figure 3.12 Simulated Brownian-motion MSD of a single bimeron for different DMI. Here, T = 40K, Ku=0.60MJ/m^3.

The competition between perpendicular magnetic anisotropy (PMA) and dzyaloshinskii-Moriya interaction (DMI) determine the stabilization of chiral spin textures, thus we increased the strength of both PMA and DMI. As shown in figure 3.12, The size of the simulated sample is a circular nanodot of diameter 2 R_d = 120nm and thickness of 1 nm. Here are the following material parameters: $M_s = 47e\text{^}4\ A/m$, $A = 15pJm^{-1}$, $alpha$ = 0.03. When PMA was constant, MSD decreased significantly with the increase of DMI strength.

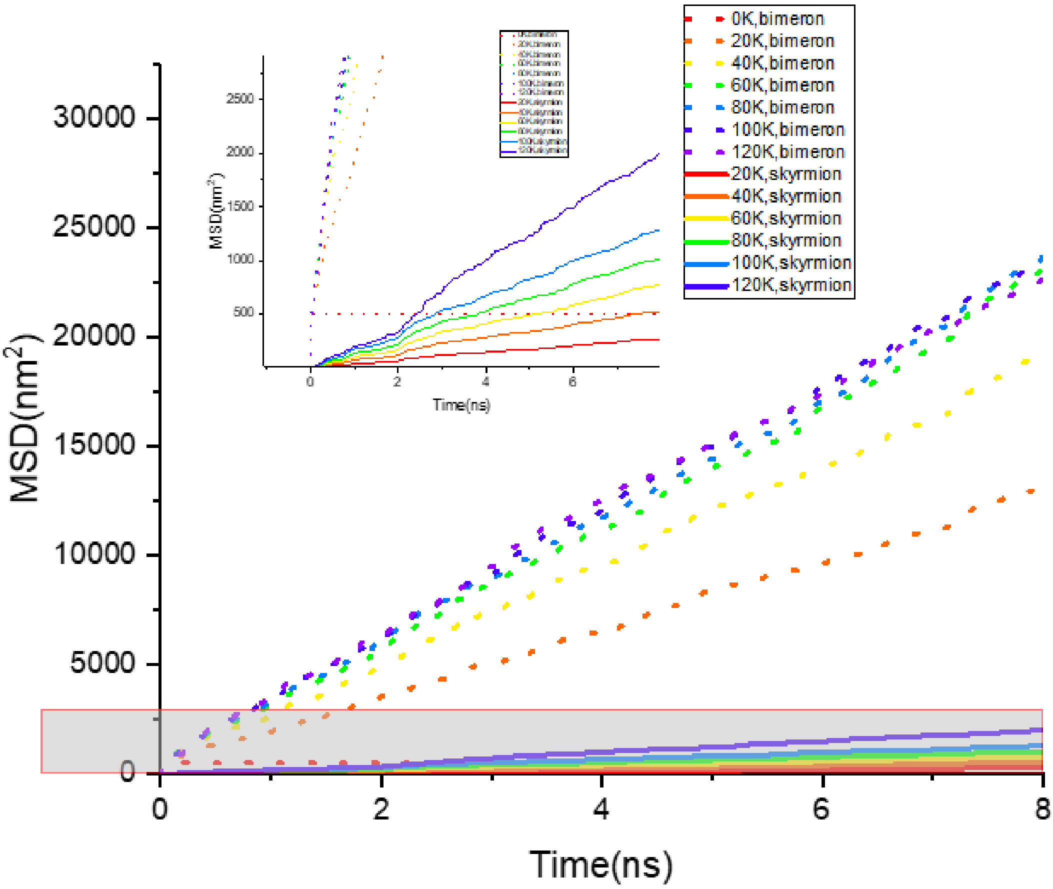

Figure 3.13 Simulated and compared Brownian-motion MSD of bimeron and skyrmion at different temperature. The dot lines represents bimeron, while the solid line represents skyrmion. Here, Ku=0.40MJ/m^3, D=3.5mJ/m^2.

Figure 3.13 compares MSD between skyrmion and bimeron at different temperature. Brown movement of bimeron under thermal effects is more intense than skyrmion, on the same size of circular nanodot of diameter 2 R_d = 120nm and thickness of 1 nm, and material parameters: $M_s = 47e\text{^}4\ A/m$, $A = 15pJm^{-1}$, $alpha$ = 0.05.

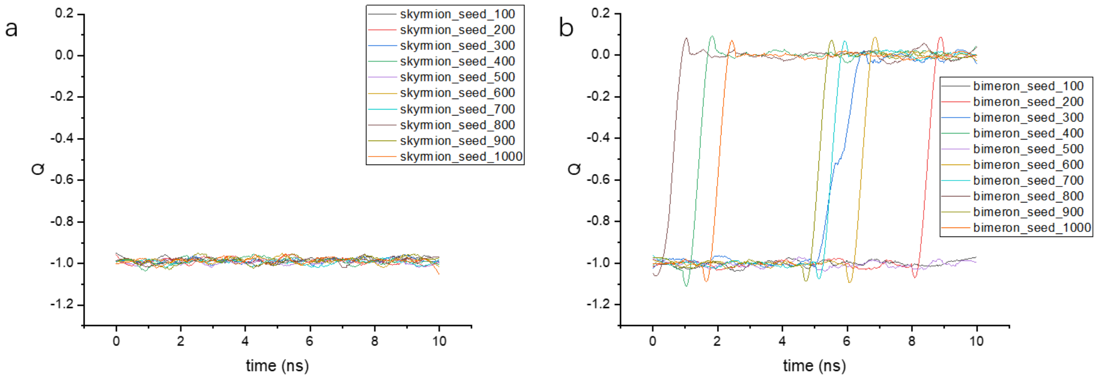

Figure 3.14 (a) Number of skyrmion topologies on average. (b) Number of bimeron topologies on average.

Figure 3.14 displays the average topology number for skyrmion and bimeron under different random seeds (100-1000). Exchange constant $A = 15pJm^{-1}$, saturation magnetization $M_s = 47e\text{^}4\,A/m$, A vertical magnetic anisotropy constant $Ku = 0.6e\text{^}6J/m^3$, an interfacial Dzyaloshinskii-Moriya interaction (DMI) constant $D = 0.6e\text{^}6\,j/m^2$, gilbert damped αlpha= 0.08. Currently, the temperature is 100 k. Figure 3.14 shows that the topological number of skyrmion remains stable near -1. Annihilation of the bimeron occurs when seed is 200, 300, 400, 600, 700, 800, 900, 1000. As a result, bimeron's thermal effect has a significant impact on the structure and its thermal stability is less than skyrmion's.

3. 3 Summary

As discussed in this chapter, we calculate the instantaneous displacement, instantaneous velocity, and the MSD for the skyrmion and bimeron respectively, as well as the influence of DMI on the MSD for the bimeron. Additionally, the MSD and topology numbers of skyrmion and bimeron are compared. Under thermal effect, it is obvious that bimeron is more effective than skyrmion. In combination with figures 3.6 and 3.14, each meron will shift in a different direction under the influence of thermal effect, which is one of the reasons for the poor thermal stability of bimeron.

Cheater.4 Summary and future work

4. 1 Summary

Skyrmion-based devices have the potential to be used in future digital computing devices. Recent research has focused on skyrmion, while bimeron has been relatively infrequently studied as its in-plane counterpart. Through simulation experiments, skyrmion and bimeron are stabilized in the same environment and the thermal Brownian motion and thermal stability of the two particles are compared by comparing experimental phenomena and quantitative experimental results.

In Chapter 2, we calculate the topological number of skyrmion and bimeron under thermal effect, respectively, by finite difference methods and lattice-based methods and conclude that the difference between the finite difference derivative method and the lattice-based method is small. There is, however, a large difference between the topology number of bimeron based on the finite-difference derivative method and the actual experimental results. Thus, we chose the lattice-based method for determining the topology number of the bimeron and achieved positive results. By calculating topological numbers, we can better understand the effects of thermal fluctuations on particles, such as nucleation, annihilation, or magnetic domains.

As we illustrate in Chapter 3, skyrmion and bimeron demonstrate thermal Brownian motion, and bimeron calculates the trajectory and velocity of each of the two merons. It is explained that the two merons in the bimeron are of varying trajectories and velocities based on the experimental data obtained and compared to the skyrmion data. Furthermore, the different activities of skyrmion and bimeron under thermal effect were quantified by MSD(mean-squared displacement). By comparing the two kinds of particles, the different effects of thermal effects on skyrmion and bimeron are demonstrated.

4. 2 Future work

For further research purposes, it is suggested that the following ideas could be considered. I will continue my research after the MSc study.

Machine learning in skyrmion

An increasing number of modern devices rely on machine learning in order to build smart, energy-efficient societies. One of the most popular applications of artificial intelligence is in the area of audio and facial recognition. Researchers have analyzed large data sets in micromagnetism by training models that can be used to categorize observations into discrete groups, determine performance indicators, or predict the results of new experiments. The algorithms for machine learning are designed to solve various types of problems and then are trained for specific tasks based on the types of data available. The process of supervised machine learning requires the labeling of the input data, usually by the characteristics of the data. The trained model is generally employed for prediction and classification, such as identifying and categorizing the magnetization process of skyrmion. Clustering and component analysis are usually performed using unsupervised machine learning, whereas semi-supervised machine learning can be used to refine unsupervised machine learning models. By using off-the-shelf, often open-source platforms, algorithms for common problems can be quickly applied through the work of mathematicians and computer scientists.

References

[1] C. Jin *et al.*, "High-frequency spin transfer nano-oscillator based on the motion of skyrmions in an annular groove," *New Journal of Physics,* vol. 22, no. 3, p. 033001, 2020.

[2] D. Apalkov *et al.*, "Spin-transfer torque magnetic random access memory (STT-MRAM)," *ACM Journal on Emerging Technologies in Computing Systems (JETC),* vol. 9, no. 2, pp. 1-35, 2013.

[3] S. Parkin, "Magnetic Race-Track—a Novel Storage Class Spintronic Memory," *International Journal of Modern Physics B,* vol. 22, no. 01n02, pp. 117-118, 2008.

[4] V. E. Demidov *et al.*, "Magnetic nano-oscillator driven by pure spin current," *Nature materials,* vol. 11, no. 12, pp. 1028-1031, 2012.

[5] O. Prokopenko *et al.*, "Spin-torque microwave detector with out-of-plane precessing magnetic moment," *Journal of Applied Physics,* vol. 111, no. 12, p. 123904, 2012.

[6] S. Bandyopadhyay and M. Cahay, "Electron spin for classical information processing: a brief survey of spin-based logic devices, gates and circuits," *Nanotechnology,* vol. 20, no. 41, p. 412001, 2009.

[7] T. H. R. Skyrme, "A unified field theory of mesons and baryons," *Nuclear Physics,* vol. 31, pp. 556-569, 1962.

[8] A. Belavin and A. Polyakov, "Metastable states of two-dimensional isotropic ferromagnets," *JETP lett,* vol. 22, no. 10, pp. 245-248, 1975.

[9] A. Abanov and V. L. Pokrovsky, "Skyrmion in a real magnetic film," *Physical Review B,* vol. 58, no. 14, p. R8889, 1998.

[10] U. K. Roessler, A. Bogdanov, and C. Pfleiderer, "Spontaneous skyrmion ground states in magnetic metals," *Nature,* vol. 442, no. 7104, pp. 797-801, 2006.

[11] S. Heinze *et al.*, "Spontaneous atomic-scale magnetic skyrmion lattice in two dimensions," *nature physics,* vol. 7, no. 9, pp. 713-718, 2011.

[12] S. Chen *et al.*, "Dynamic response for Dzyaloshinskii–Moriya interaction on bubble-like magnetic solitons driven by spin-polarized current," *Journal of Physics D: Applied Physics,* vol. 49, no. 19, p. 195004, 2016.

[13] S. Zhang *et al.*, "Current-induced magnetic skyrmions oscillator," *New Journal of Physics,* vol. 17, no. 2, p. 023061, 2015.

[14] C. Jin *et al.*, "Array of synchronized nano-oscillators based on repulsion between domain wall and skyrmion," *Physical Review Applied,* vol. 9, no. 4, p. 044007, 2018.

[15] V. D'Alfaro, G. Furlan, and S. P. Fubini, "A new classical solution of the Yang-Mills field equations," *Phys. Lett. B,* vol. 65, no. CERN-TH-2232, pp. 163-166, 1976.

[16] C. Phatak, A. Petford-Long, and O. Heinonen, "Direct observation of unconventional topological spin structure in coupled magnetic discs," *Physical review letters,* vol. 108, no. 6, p. 067205, 2012.

[17] S. Wintz *et al.*, "Topology and origin of effective spin meron pairs in ferromagnetic multilayer elements," *Physical review letters,* vol. 110, no. 17, p. 177201, 2013.

[18] A. Araújo *et al.*, "Typical skyrmions versus bimerons: A long-distance competition in ferromagnetic racetracks," *Physical Review B,* vol. 102, no. 10, p. 104409, 2020.

[19] N. Romming *et al.*, "Writing and deleting single magnetic skyrmions," *Science,* vol. 341, no. 6146, pp. 636-639, 2013.

[20] C. Moreau-Luchaire *et al.*, "Additive interfacial chiral interaction in multilayers for stabilization of small individual skyrmions at room temperature," *Nature nanotechnology,* vol. 11, no. 5, pp. 444-448, 2016.

[21] W. Jiang *et al.*, "Blowing magnetic skyrmion bubbles," *Science,* vol. 349, no. 6245, pp. 283-286, 2015.

[22] L. Zhao *et al.*, "Topology-dependent brownian gyromotion of a single skyrmion," *Physical review letters,* vol. 125, no. 2, p. 027206, 2020.

[23] A. Vansteenkiste, J. Leliaert, M. Dvornik, M. Helsen, F. Garcia-Sanchez, and B. Van Waeyenberge, "The design and verification of MuMax3," *AIP advances,* vol. 4, no. 10, p. 107133, 2014.

[24] M. N. Baibich *et al.*, "Giant magnetoresistance of (001) Fe/(001) Cr magnetic superlattices," *Physical review letters,* vol. 61, no. 21, p. 2472, 1988.

[25] A. Fert, "Origin, development, and future of spintronics (Nobel lecture)," *Angewandte Chemie International Edition,* vol. 47, no. 32, pp. 5956-5967, 2008.

[26] S. S. Parkin *et al.*, "Giant tunnelling magnetoresistance at room temperature with MgO (100) tunnel barriers," *Nature materials,* vol. 3, no. 12, pp. 862-867, 2004.

[27] M. d'Aquino, "Nonlinear magnetization dynamics in thin-films and nanoparticles," *http://wpage. unina. it/mdaquino/PhD_thesis/main/main. html,* 2004.

[28] T. Moriya, "Anisotropic superexchange interaction and weak ferromagnetism," *Physical review,* vol. 120, no. 1, p. 91, 1960.

[29] I. Dzyaloshinsky, "A thermodynamic theory of "weak" ferromagnetism of antiferromagnetics," *Journal of physics and chemistry of solids,* vol. 4, no. 4, pp. 241-255, 1958.

[30] J. Walowski, "Non-local/local gilbert damping in nickel and permalloy thin films," 2007.

[31] T. Gilbert and J. Kelly, "Anomalous rotational damping in ferromagnetic sheets," in *Conf. Magnetism and Magnetic Materials, Pittsburgh, PA*, 1955, pp. 253-263.

[32] A. Turrin, "Quantum-mechanical form of the damped bloch equations," *Physics Letters A,* vol. 59, no. 6, pp. 423-425, 1977.

[33] E. Barati, M. Cinal, D. Edwards, and A. Umerski, "Calculation of Gilbert damping in ferromagnetic films," in *EPJ Web of Conferences*, 2013, vol. 40: EDP Sciences, p. 18003.

[34] A. Fert, V. Cros, and J. Sampaio, "Skyrmions on the track," *Nature nanotechnology,* vol. 8, no. 3, pp. 152-156, 2013.

[35] N. Nagaosa and Y. Tokura, "Topological properties and dynamics of magnetic skyrmions," *Nature nanotechnology,* vol. 8, no. 12, pp. 899-911, 2013.

[36] J. Sampaio, V. Cros, S. Rohart, A. Thiaville, and A. Fert, "Nucleation, stability and current-induced motion of isolated magnetic skyrmions in nanostructures," *Nature nanotechnology,* vol. 8, no. 11, pp. 839-844, 2013.

[37] H. Du, W. Ning, M. Tian, and Y. Zhang, "Field-driven evolution of chiral spin textures in a thin helimagnet nanodisk," *Physical Review B,* vol. 87, no. 1, p. 014401, 2013.

[38] Z.-A. Li *et al.*, "Magnetic skyrmion formation at lattice defects and grain boundaries studied by quantitative off-axis electron holography," *Nano letters,* vol. 17, no. 3, pp. 1395-1401, 2017.

[39] C. Jin *et al.*, "Control of morphology and formation of highly geometrically confined magnetic skyrmions," *Nature communications,* vol. 8, no. 1, pp. 1-9, 2017.

[40] Y. Bai, D. Xu, L. Mao, J. Guo, and H. Fu, "FEM/FDM-joint simulation for transport phenomena in directionally solidifying shaped TiAl casting under electromagnetic field," *ISIJ international,* vol. 44, no. 7, pp. 1173-1179, 2004.

[41] J. E. Miltat and M. J. Donahue, "Numerical micromagnetics: Finite difference methods," *Handbook of magnetism and advanced magnetic materials,* vol. 2, pp. 742-764, 2007.

[42] J.-V. Kim and J. Mulkers, "On quantifying the topological charge in micromagnetics using a lattice-based approach," *IOP SciNotes,* vol. 1, no. 2, p. 025211, 2020.

[43] B. Berg and M. Lüscher, "Definition and statistical distributions of a topological number in the lattice O (3) σ-model," *Nuclear Physics B,* vol. 190, no. 2, pp. 412-424, 1981.

[44] R. Rajaraman, "An Introduction to Solitons and Instantons in Quantum Field Theory, Solitons and Instantons, Vol. 15," ed: North Holland Personal Library, Elsevier Science, Amsterdam, 1987.

[45] T. H. R. Skyrme, "A non-linear field theory," in *Selected papers, with commentary, of Tony Hilton Royle Skyrme*: World Scientific, 1994, pp. 195-206.

[46] H.-B. Braun, "Topological effects in nanomagnetism: from superparamagnetism to chiral quantum solitons," *Advances in Physics,* vol. 61, no. 1, pp. 1-116, 2012.

[47] G. P. Müller *et al.*, "Spirit: Multifunctional framework for atomistic spin simulations," *Physical Review B,* vol. 99, no. 22, p. 224414, 2019.

[48] M. Böttcher, S. Heinze, S. Egorov, J. Sinova, and B. Dupé, "B–T phase diagram of Pd/Fe/Ir (111) computed with parallel tempering Monte Carlo," *New Journal of Physics,* vol. 20, no. 10, p. 103014, 2018.

[49] Y. Yao, X. Chen, W. Kang, Y. Zhang, and W. Zhao, "Thermal brownian motion of skyrmion for true random number generation," *IEEE Transactions on Electron Devices,* vol. 67, no. 6, pp. 2553-2558, 2020.

[50] A. J. Menezes, P. C. Van Oorschot, and S. A. Vanstone, "Applied cryptography," *CRC, Boca Raton,* 1996.

[51] J. Han, H. Chen, J. Liang, P. Zhu, Z. Yang, and F. Lombardi, "A stochastic computational approach for accurate and efficient reliability evaluation," *IEEE Transactions on Computers,* vol. 63, no. 6, pp. 1336-1350, 2012.

[52] H. Çakallı, "Upward and downward statistical continuities," *Filomat,* vol. 29, no. 10, pp. 2265-2273, 2015.